Med-X (2025) 3:8
https://doi.org/10.1007/s44258-024-00049-9

Med-X

REVIEW

Optical imaging unveiling metabolic dynamics in cells and organisms during aging and diseases

Lingyan Shi[1] · Jorge Villazon[1]

Received: 16 August 2024 / Revised: 17 October 2024 / Accepted: 10 December 2024

Abstract

Cellular metabolism plays a critical role in various physiological and pathological processes. High resolution imaging of intracellular metabolic activities is crucial for understanding many biological pathways, and for facilitating disease prognosis and treatment assessment. Raman scattering (RS) spectroscopy/microscopy, in particular stimulated Raman scattering (SRS), has emerged as a powerful imaging technology for cellular imaging with high specificity, high sensitivity, and subcellular resolution. Since its invention, SRS microscopy imaging has been extensively applied in life science for studying composition, structure, metabolism, development, and disease in biological systems. This review focuses on the latest applications of SRS imaging, particularly with heavy water probing, for studying metabolic dynamics of biomolecules in organisms during aging and diseases. Furthermore, future applications and development of SRS imaging in both life science and medicine are considered.

Graphical Abstract

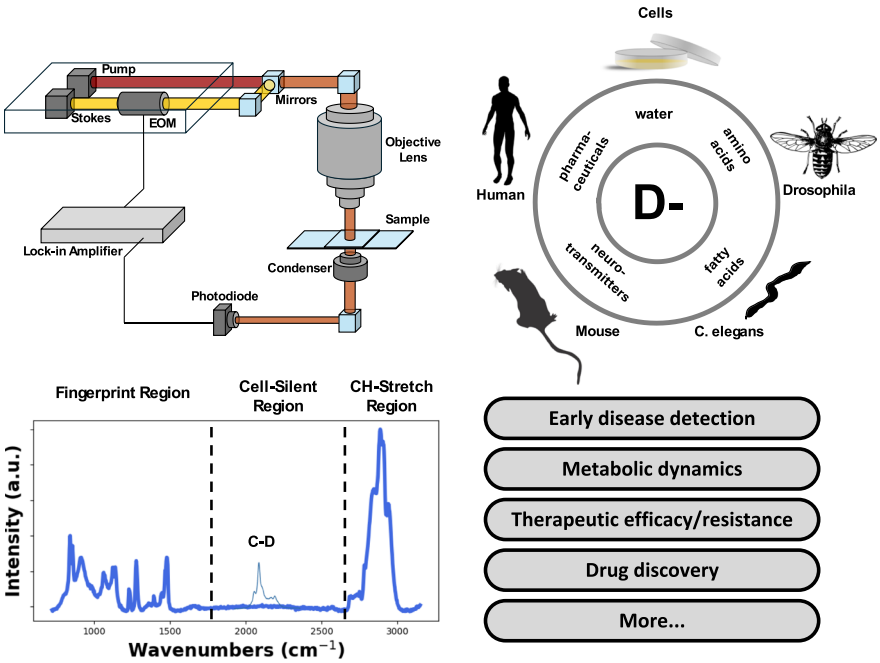

Extended author information available on the last page of the article

Published online: 20 February 2025

Springer

Highlights

- Stimulated Raman scattering microscopy with heavy water probing can be leveraged for imaging vibrational "tags" of molecular bonds.
- The labeling of the carbon-deuterium bonds provides a measurable marker for biomolecule synthesis, particularly for proteins and lipids.
- These metabolic markers can be vital to understanding physiological processes, such as in aging, age-related diseases and cancer.
- The application of this metabolic imaging platform has elicited novel findings on the role of protein and lipid synthesis and turnover.

Keywords Metabolic imaging · Raman scattering · Aging · Neurodegeneration · Cancer

Introduction

The metabolic dynamics of biomolecules, such as lipids and protein, are crucial in the physiological and pathological processes in an organism. Metabolic imaging provides a powerful tool for tracking and quantifying biomolecular metabolism, which is important for probing alterations in metabolic pathways, understanding the underlying mechanisms, and for diseases diagnosis and treatment evaluation. However, high resolution and high sensitivity imaging tools for mapping these metabolic activities are limited. Conventional imaging techniques implemented in clinics include positron emission tomography (PET), magnetic resonance spectroscopy (MRS), and mass spectrometry (MS)-based imaging such as matrix-assisted laser desorption/ionization (MALDI)-MS. These methods have inherent limitations such as low spatial resolution (PET), low sensitivity and spectral resolution (MRS), long sample preparation time (MS), or destruction of live tissues (MALDI-MS).

Optical imaging technologies leverage visible or near-infrared light that provide a direct, non-invasive means to study biological processes in cells and organisms. Of note is fluorescence microscopy imaging, an important and well-known method of imaging living biological systems. Compared to the aforementioned technologies, fluorescence microscopy has high spatiotemporal resolution. However, fluorescence microscopy is limited due to photo-toxicity and the bulky fluorescent probes often required, which can possibly disturb the native environment in cell and tissues. An exception is the multiphoton autofluorescence imaging of endogenous fluorophores, typically, reduced nicotinamide adenine dinucleotide (NADH) and flavin adenine dinucleotide (FAD), in living systems [1–3]. Quantitative measurements of the changes in NADH and FAD can reveal cellular metabolic and differentiation state.

Raman spectroscopy/microscopy, another popular optical imaging method, was first applied in living organisms in the 2000s [4–6]. Raman spectroscopy/microscopy utilizes a visible or near-infrared light source and measures the inelastic scattering of light by vibrating chemical bonds within a molecule. Different chemical bonds in a molecule vibrate at different frequencies, offering unique fingerprints of the molecule in the Raman spectrum. Due to this property, Raman imaging technology offers high chemical specificity and sensitivity. Another advantage of the normal (spontaneous) Raman is that the signal intensity measured is linearly proportional to the amount of chemical bonds inside cells, which allows for quantitative analysis. Since metabolic activities inside cells and tissues are altered during aging and diseases, even before morphological changes are visible, Raman spectroscopy provides an effective method for early detection and diagnosis of diseases.

Raman spectroscopy is one example of a vibrational spectroscopy modality, another being infrared (IR) spectroscopy. IR spectroscopy was first utilized for imaging a biological specimen in the 1990s [7, 8]. Unlike Raman imaging, IR spectroscopy measures the absorption of light in the IR region due to the dipole moment of bonds within a molecule, i.e., the unequally sharing of electrons within a bond. Different bonds within the molecule exhibiting a dipole moment will absorb the light at different wavenumbers, generating different fingerprints which are detected based on the absorbance of specific peaks in the IR spectrum. IR spectroscopy has robust signal in the fingerprint region but is limited in live cell imaging due to strong water absorption in the IR spectrum.

The signal intensity in spontaneous Raman is very weak that necessitating a long imaging time (low speed), which limits its applications for metabolic imaging of living cells and organisms. Therefore, variants of Raman imaging modalities have been developed for metabolic imaging, such as stimulated Raman scattering (SRS) and coherent anti-Stokes Raman scattering (CARS). As a relatively new imaging technique, SRS microscopy was first developed and applied for bioimaging in 2008 [6]. It has advanced rapidly as a powerful tool for metabolic imaging since the past decade. SRS is a nonlinear process that uses two synchronized pulsed lasers, the pump beam and the Stokes beam. When the frequency difference between the pump beam and Stokes beam equals the vibrational frequency of a chemical bond

within a molecule, the intensity in the Stokes beam increases (stimulated Raman gain, SRG) and the intensity in the pump beam decreases (stimulated Raman loss, SRL). Either SRG or SRL can be detected by SRS spectroscopy. Compared with spontaneous Raman, SRS signal intensity is several orders of magnitude higher, thus, providing faster imaging speed (over 1000 times) [9]. In addition, SRS microscopy can achieve a spatial resolution up to 100 nm, a temporal resolution of ~1 μs/pixel, and chemical sensitivity of ~1 μM. It also enables both multiplex and 3D volumetric imaging [10]. SRS signal appears at the same frequency (wavenumber) as the excitation beam; therefore, it shares the same spectral profile as the spontaneous Raman, and the signal intensity is also linearly proportional to the content of the molecule, enabling quantitative measurement of metabolites. In common practice, spontaneous Raman spectroscopy is used for scanning the whole vibrational spectrum, and SRS imaging captures a single wavenumber corresponding to a specific type of biomolecule. Details of SRS imaging principles, modalities, and applications have been well reviewed in references [10–14].

Raman imaging is inherently label-free, circumventing the need for bulky probes like those in fluorescence microscopy. It detects chemical bond (e.g., C-H, C = C, O–P–O) vibration in the fingerprint region (wavenumber 400 – 1800 cm^{-1}) and C-H stretch region (2800 – 3100 cm^{-1}) of the Raman spectrum. However, in the fingerprint region different molecules usually share the same chemical bonds, leading to spectral overlapping, making it difficult to identify and quantify each of the molecules, thus limiting the molecular specificity and sensitivity of imaging. Hence, the whole Raman spectrum is probed from the fingerprint to the C-H stretch region for accurate identification of the biomolecular species. But still, the C-H stretch region does not have sufficient features for discrimination. In addition, label free Raman imaging can only provide information of a steady state, i.e., measure the total content of a species, but cannot reveal metabolic turnover of the species.

For this reason, vibrational probes have been developed to increase imaging contrast [15]. Vibrational probes are chemical groups or specific isotopes that generate a Raman shift in scattered photons at specific frequencies, of which, the most utilized for metabolic imaging typically include stable isotope (deuterium and ^{13}C) and triple-bond (alkyne). These probes will replace the original bonds (e.g., C-H) within the endogenous molecules by generating new bonds such as C-D and C-N, with characteristic vibrational frequencies falling within the Raman cell-silent region (1800 – 2800 cm^{-1}), a region which negligible signal from molecules commonly present in cells and tissue. Integrating vibrational probes not only enhances the chemical specificity, but also allows for tracking and quantifying metabolic dynamics/turnovers of labeled biomolecules that is impossible in label-free imaging. Stable isotopes (deuterium, ^{13}C) are the smallest labels such that they induce no or little perturbation to the native environment inside cells, of these the main isotope label used with Raman imaging is deuterium (D). When the deuterium label is incorporated into the molecules, certain amount of C-H bonds in the molecules will be replaced by C-D bonds during molecular metabolism, and the corresponding characteristic vibrational frequency is shifted from the C-H stretch region (~ 2900 cm^{-1}) to the cell-silent region (~ 2100 cm^{-1}). For example, D-labeled newly synthesized lipids (containing C-D bonds) display a Raman peak at 2135 cm^{-1}, while a peak at 2845 cm^{-1} corresponds to the total lipids (C-H bonds) [16]. Thus, by probing the C-D and C-H peaks, lipids metabolic turnover (ratio of C-D to C-H) can be revealed and quantified. For deuterium labeling, a direct way is to use deuterated probes for the corresponding molecules of interest, such as using deuterated amino acids (d-AA) for metabolic imaging of protein in live cells and organisms [17, 18], deuterated fatty acid (d-FA) for visualizing lipogenic activities in living tissues [19], deuterated cholesterol for visualizing cholesterol storage in lipid droplets [20], and deuterated choline for mapping metabolites containing choline in cells and *C. elegans* [21]. This method is, however, limited in that each probe can only label one type of molecule.

To probe metabolic activities in multiple species, different types of probes are generally needed. However, one study using only a single probe, D-labeled glucose (D_7-glucose), and with spectral tracing of deuterium isotopes (STRIDE), successfully traced the allocation of glucose anabolic products toward the syntheses of various biomolecules including lipids, protein, nucleic acids, and glycogen (Fig. 1) [22]. A novel approach was further proposed for metabolic imaging of multiple biomolecules simultaneously. Using heavy water (D_2O) as a universal label for SRS imaging (DO-SRS), metabolic dynamics of lipids, protein, and DNA were imaged in animals in situ, metabolism of lipids and protein were also visualized simultaneously in animal (Fig. 1) [16]. D_2O label displays many advantages compared with deuterated labels. As an isotopologue of water, D_2O can freely travel across organelle membranes and diffuse in cells, equilibrate with body water within an organism and label newly synthesized biomolecules through metabolism. D_2O labeling displays higher labeling efficiency, does not perturb native metabolism, is nondestructive and is a non-carbon tracer that can probe de novo biosynthesis, providing a significant advantage over co similar probes. While cellular uptake of d-FA may lead to bias in different cell types, this does not occur with D_2O probing. In addition, D_2O labeling enables simultaneous visualization of lipid and protein metabolism in cells. For these reasons, DO-SRS imaging is an ideal and powerful tool for studying aging and diseases.

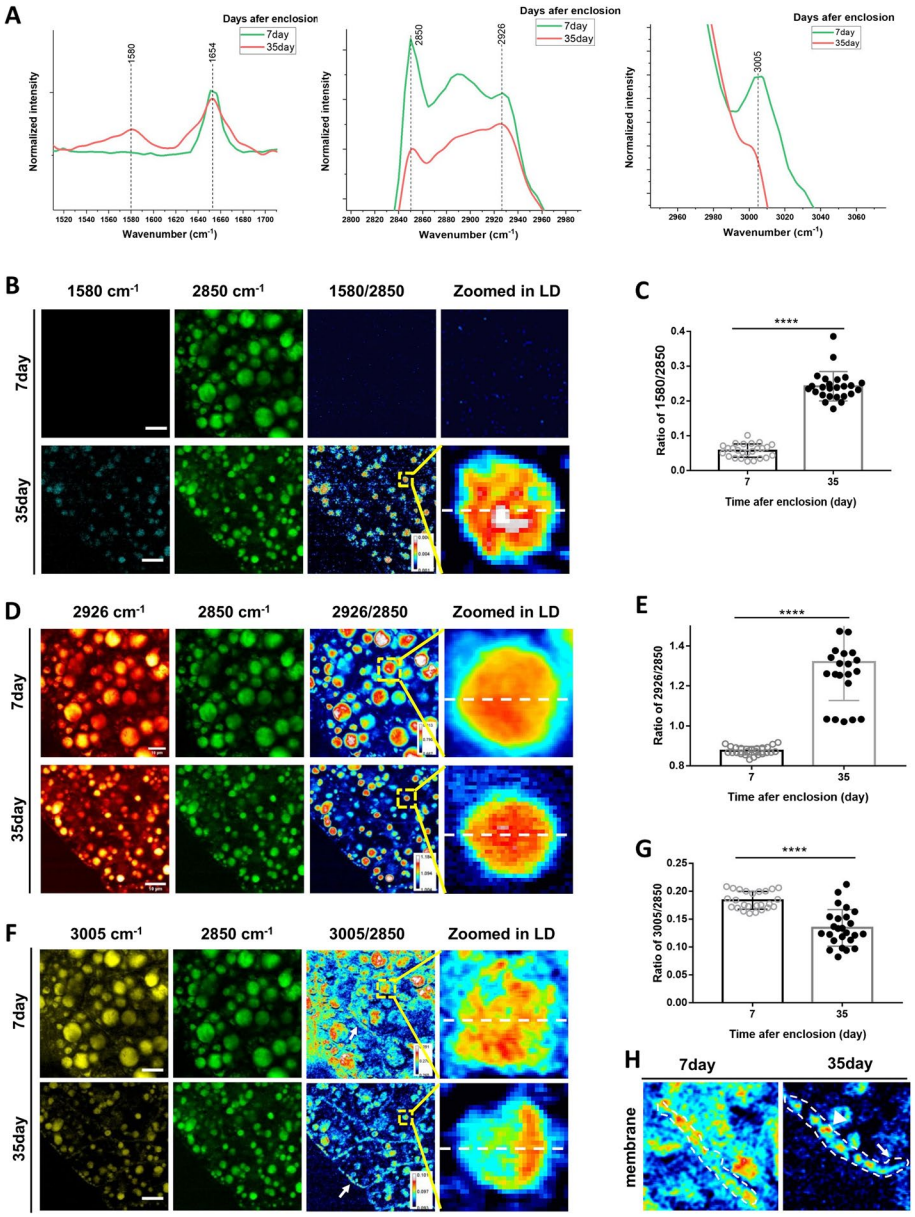

Fig. 1 SRS imaging detection of biomolecular changes in LDs. SRS images demonstrate more and larger LDs in young flies and smaller LDs were observed in old flies. **A** Raman spectra of the fat body in young (7-day) flies and old (35-day) flies at 1580 cm^{-1} (retinoid C=C), 2850 cm^{-1} (CH2 stretching of lipids), 2926 cm^{-1}, and 3005 cm^{-1} (unsaturated fatty acids). **B** SRS images of retinoids in the fat bodies of young and old flies. Ratiometric images of 1580 cm^{-1} to 2850 cm^{-1} show a significant increase of retinoids in old flies. Retinoids were not detectable in young flies. **C** Quantification of changes in retinoids relative to lipids in young and old flies. There was a significant increase in retinoids in old flies. **D** SRS images of 2926 cm^{-1} in the fat bodies of young and old flies. Ratiometric images of 2926 cm^{-1} to 2850 cm^{-1} demonstrate significantly stronger intensity in old flies, indicating more protein synthesis. **E** Quantification of protein changes relative to lipids in young and old flies. The relative content of proteins significantly increased in old flies. **F** SRS images of unsaturated FAs (at 3005 cm^{-1}) in young and old flies. Ratiometric images of unsaturated FAs to lipids (at 2850 cm^{-1}) show weaker signals in old flies, indicating the reduction of unsaturated FAs. Unsaturated FAs were more located in certain regions inside the LD in old flies. **G** Quantification of changes in unsaturated FAs in young and old flies. In old flies, unsaturated FAs decreased significantly. **H** Ratiometric images of unsaturated FAs near/on the fat body cell membrane. More unsaturated FAs were localized on the membrane in young flies. Results are presented as mean ± SD ($n=25$ in each group). Statistical significance was determined by using unpaired Student's t-test. ****, $p<0.0001$. Adapted from reference (Li et al., 2021) [23]

Extensive work using Raman for metabolic imaging has been conducted since the past decades. The development and applications of Raman (including spontaneous, CARS, and SRS) metabolic imaging of cells, tissues, and organisms have been well documented and thoroughly

reviewed most recently [14, 24–30]. This review will focus on the latest advances and applications of SRS and DO-SRS imaging of organisms for studying metabolic dynamics/turnover in aging and cancer without the introduction of large exogenous probes. Due to the scope, there may be studies regrettably uncovered. The first section will review applications of DO-SRS imaging for studies on aging. Then, studies on metabolic activities in diseases, such as neurodegenerative diseases and cancer, will be reviewed. Finally, challenges and perspectives of metabolic imaging in studying aging and diseases will be discussed.

DO-SRS imaging of metabolic activities in studying aging

Aging is associated with progressive decline of physiological functions and increased susceptibility to death [31]. It is also a major risk factor for diseases including cancer, diabetes, cardiovascular diseases, and neurodegenerative diseases such as Alzheimer's disease (AD) and Parkinson disease (PD) [32]. Recent studies have suggested that lipid metabolism is not only associated with but crucial in regulating aging and age-related diseases [33]. Lipids play important roles in energy storage and mobilization. They are also fundamental components of cell/organelle membranes and messengers in signaling pathways [34]. However, it remains unclear how lipid metabolism impacts aging process. Unveiling the role of lipid in aging will improve the identification of pharmaceutical targets and design of therapeutic approaches for improving aging and treating age-related diseases.

Conventional methods for lipidomic analysis are usually mass spectrometry (MS)-based, which either lack spatial information of lipids inside cells, or are invasive and have low resolution and imaging depth [35, 36]. Thus, high resolution optical imaging for trace lipid metabolic dynamics in live cells and organisms in situ is highly desired. Heavy water probed SRS (DO-SRS) imaging proposes a novel and potent approach.

Many studies on aging have investigated the lifespan in short-lived model organisms. *Drosophila* (fruit fly) is one of those most-commonly used, with advantages including short lifespan (40–50 days), having homolog with ~ 65% of human disease-causing genes [37], and genetically amendable. By examining the lifespan change subjected to genetic, pharmacological, or dietary manipulation on *Drosophila*, the molecular mechanisms in human disease phenotypes, such as the insulin/insulin-like growth factor (IGF) and insulin signaling pathway, can be rapidly investigated.

DO-SRS imaging of metabolic dynamics in aging Drosophila

The novel DO-SRS microscopy imaging platform was used to study metabolic activities during *Drosophila* aging. This study was the first that directly visualized the spatiotemporal lipids and protein metabolic dynamics in fly fat body at subcellular scale for studying aging [23].

Validation of SRS and DO-SRS metabolic imaging of Drosophila fat body

The *Drosophila* fat body is an analog to human adipose tissue (energy storage) and liver (metabolism, glycogen storage, and nutrient sensing) in mammals [38]. Label free SRS imaging and Raman spectroscopy were first performed to identify and track biomolecule metabolism at steady state in 7-day (young) and 35-day (old) adult *Drosophila* fat body. Four Raman peaks of interest were detected: two peaks at 1580 and 3005 cm^{-1} were from retinoids and unsaturated fatty acids (FAs) [39], respectively, and the other two peaks at 2850 and 2926 cm^{-1} for CH_2 stretching of lipids and proteins, respectively (Fig. 1A). Ratiometric images were generated by dividing all images by the lipids at 2850 cm^{-1}. SRS imaging found that retinoids level was significantly high in old (35-day) flies but was barely seen in young (7-day) flies, indicating old flies accumulated a large amount of retinoids in the fat body (Fig. 1B-G). Old flies also displayed more protein contents than lipids in the fat body, most likely due to decreased lipid storage, and significantly reduced unsaturated lipids on the fat body cell membrane (Fig. 1H); while young flies showed similar levels of protein and lipids in the fat body, and more scattered unsaturated FAs inside lipid droplets (LDs), which were more concentrated in one area in old flies.

As a validation of the DO-SRS imaging platform for metabolic imaging, the optimal concentration of D_2O was first determined for optimal in vivo labeling in Drosophila. For this purpose, flies were fed standard food mixed with different concentrations (0 – 100%) of D_2O for 24 h. Raman spectra of 20–30 randomly chosen fat body regions from different flies were collected. A distinct peak at 2143 cm^{-1} was observed, corresponding to the C-D bonds in newly-synthesized lipids. The signal strength increased with D_2O concentration until 30%, and then started to decline, indicating saturation of deuterium in the body and potentially inhibitory effect at higher concentrations of D_2O. This was verified by lifespan experiments in which male flies that were fed 30% D_2O-containing food displayed a shortened lifespan, while there was no significant changes in female flies. But for flies fed 10% and 20% D_2O, there was no gender difference in lifespan. Therefore, 20% D_2O was selected

for in vivo labeling. In addition, 5-day D_2O treatment was found to obtain stable and detectable signal.

Then the metabolism in 3-day fly fat body LDs was imaged using DO-SRS. In *Drosophila*, after digestion and absorption, lipids in the food will first enter the hemolymph and be transported to the fat body and stored in the LDs. Therefore, the size and number of LDs may serve as indicators of the metabolic level in fat body cells. After treatment of 20% D_2O for 5 days, metabolic dynamics of lipids in 3-day fly LDs were visualized by SRS microscopy in situ. Ratiometric images of C-D (2143 cm^{-1}) to C-H (2850 cm^{-1}) lipids revealed non-uniform lipid metabolism occurring inside LDs, and significantly higher turnover in large LDs (diameter > 4 μm) than small LDs (diameter < 4 μm), indicating more active metabolism in large LDs, while large and small LDs play different roles in maintaining cellular homeostasis.

DO-SRS imaging of lipid and protein metabolic activities in aging Drosophila

For the aging study, female flies at multiple ages were investigated. Previous studies reported changing lipid profiles with age in many animal models [40–43] and increased uptake of lipids extending lifespan in *C. elegans* [41]. These studies, however, were based on mass spectrometry that is destructive and cannot provide spatial information.

With the DO-SRS imaging platform this limitation can be overcome. Female flies at ages of 2-, 10-, 20-, and 30-day were fed 20% D_2O-containning food for 5 days (hence, 7-, 15-, 25-, and 35-day old), and then subjected to Raman spectroscopy and SRS imaging to assess lipids and protein turnover in the fat body. A distinct peak at 2143 cm^{-1} was observed in all age groups except the 35-day group, indicating significantly decreased metabolic turnover in old flies (Fig. 2 A, B). The C-D peak at 2143 cm^{-1} is actually a mixture of mostly lipid and partially protein signals. To distinguish them, C-D spectra were unmixed by treating the fat body tissues with proteinase K and methanol, respectively [16]. By removing protein with proteinase K, a peak at 2141 cm^{-1} was observed, corresponding to the newly-synthesized lipids; removing lipids with methanol, a peak at 2180 cm^{-1} was obtained, correspondingly, newly-synthesized protein. In addition, Raman spectra displayed a pattern more lipid-like in younger flies while more protein-like in old flies, suggesting loss of lipid storage in aging flies (Fig. 2C, D).

Lipid and protein turnovers were quantified by the ratios of newly-synthesized lipid/protein (C-D) to total lipid/protein (C-H), specifically, signals at 2141 cm^{-1} to 2850 cm^{-1}, and 2180 cm^{-1} to 2929 cm^{-1}, respectively. Lipid turnover was found dramatically declined in both large and small LDs of old (35-day) flies compared with young (7-day) flies (Fig. 2E, F). More large LDs were visualized in young (7-day) flies, while in old (35-day) flies more small LDs were observed and both the total number and size of LDs were reduced, indicating drastic reduction of lipid storage in flies with aging (Fig. 2G, H). This might also cause lipotoxicity in old flies, but the large amount of retinoids observed in old flies at 1580 cm^{-1} (using label free SRS) might compensate for the loss of unsaturated FAs.

Protein turnover varied across different groups. It was increased in 15-day flies, then declined in 25- and 35-day flies. Decreases of protein turnover occurred earlier (25-day flies) than that of lipids (in 35-day flies), potentially indicating that protein metabolism may act as a prerequisite for lipid metabolism during aging. Studies have found that triglyceride absorption was impaired (up to half) in aging rodents due to lipoprotein assembly defect or a decline of fatty acid-binding proteins [44]. In addition, due to the many proteins on cell and LD membranes, protein turnover change could potentially lead to impaired lipid metabolism [45, 46].

In this study, a platform was established by employing D_2O-probed SRS imaging and a *Drosophila* model, which for the first time directly visualized the spatiotemporal metabolic dynamics of various biomolecules in situ in aging *Drosophila* at the subcellular scale. This platform provides a powerful tool for studying the interactions between metabolism and aging. In the subsequent sections, studies on aging and age-related diseases using this platform are discussed.

Diet-regulation on metabolic dynamics in aging Drosophila

One recent study applied the DO-SRS imaging platform to investigate dietary regulation of lipids metabolic activities in aging flies [47].

A typical strategy in aging study is to assess the change in animal lifespans when subjected to different kinds of interventions such as altered diet, gene manipulation, and drugs, to understand the mechanisms underlying aging. The nutrient-sensing pathways are well-known for being associated with aging and aging-related diseases [48]. These pathways include insulin/insulin-like growth factor-1 (IGF-1) and the insulin signaling pathway, mammalian target of rapamycin (mTOR), and adenosine monophosphate-activated protein kinase (AMPK) signaling pathways. They provide gene and protein targets for aging study.

DO-SRS imaging of diet regulation on Drosophila lifespan and lipid metabolic activity

The study first assessed the effects of dietary compositions on lifespan. Flies were fed foods containing different proportions of sugar and yeast (supplying protein and lipids)

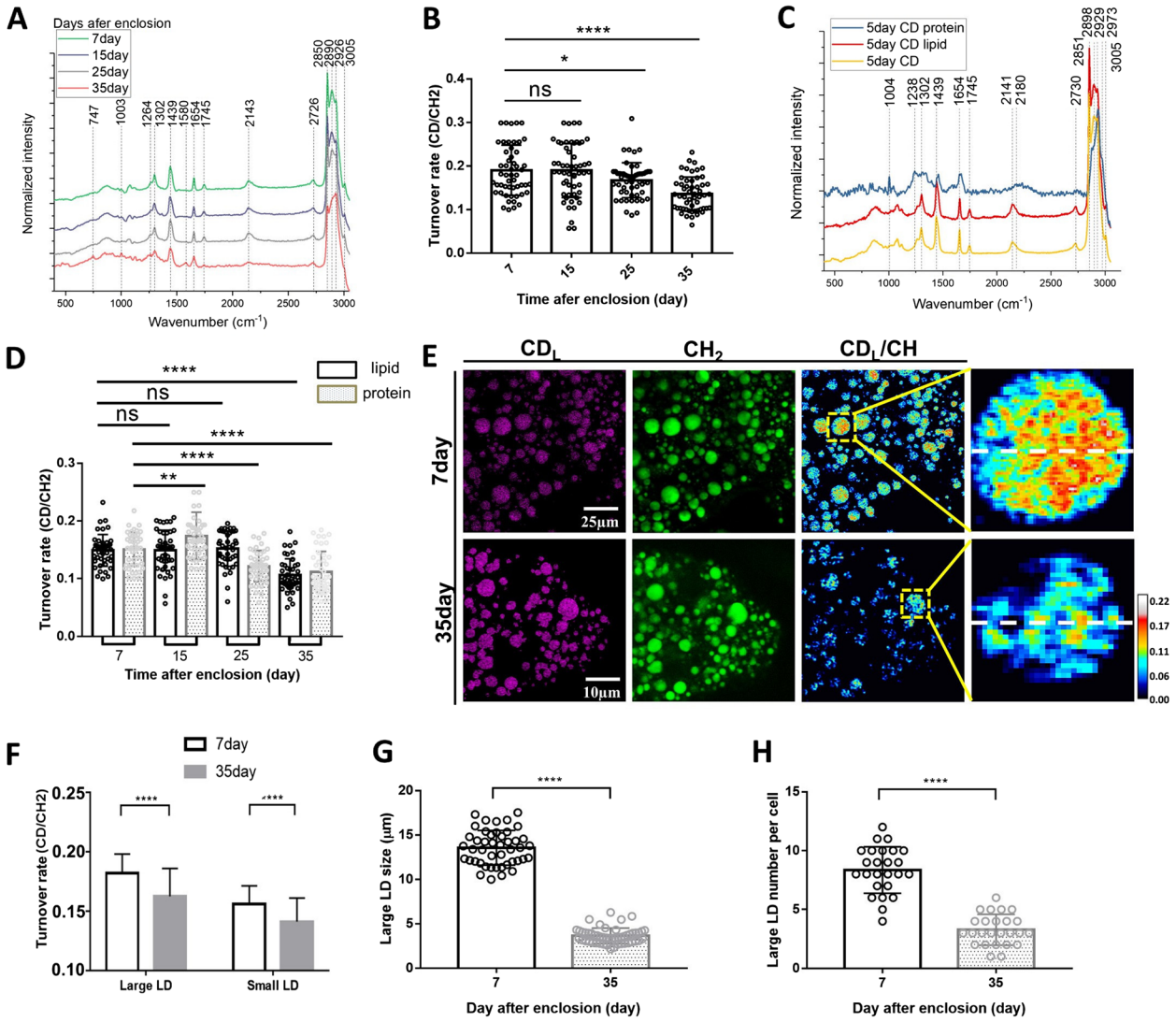

Fig. 2 The metabolic changes in the fat bodies of Drosophila during aging. **A** Averaged Raman spectra ($n=50$) were collected from flies of different ages (7, 15, 25, 35-day posteclosion). The flies were labeled by 20% D_2O label for 5 days and then imaged. **B** Quantification of the C–D turnover by dividing the intensity of 2143 cm^{-1} to the peak at 2850 cm^{-1}. **C** Unmixing of the C–D spectra into protein and lipid spectra. The peak at 2141 cm^{-1} is corresponding to the newly synthesized D-labeled lipids, and the peak at 2180 cm^{-1} is the newly synthesized D-labeled protein. **D** Quantification of lipids and protein turnover rates by 2141 cm^{-1} to 2850 cm^{-1} and 2180 cm^{-1} to 2929 cm^{-1}, respectively. **E** SRS imaging of lipid metabolic activities in 7-day (young) and 35-day (old) flies. Old flies showed reduced lipid metabolism compared with young flies. SRS imaging could visualize the lipids turnover inside single LDs at the subcellular scale. **F** Quantification of the turnover rates of large (diameter ≥ 4 μm) and small (diameter < 4 μm) LDs in the fat bodies of young and old flies. Lipid turnover rates inside both large and small LDs declined significantly in old flies. **G** Comparison of large LD size in young and old flies. **H** Comparison of large LD numbers per cell in young and old flies. Both the size and number per cell reduced drastically in old flies. Results are presented as mean ± SD ($n=50$, from 3 individuals). Statistical significance was determined by using unpaired Student's t-test. *, $p<0.05$; **, $p<0.01$; ****, $p<0.0001$; ns, non-significant difference. Adapted from reference (Li et al., 2021) [23]

including high glucose/fructose/sucrose, high/low protein, calorie restriction, and standard foods. High sugar and low protein diets were found to extend fly's lifespan while high protein shortened the lifespan, which are consistent with other studies [49, 50].

Next, to elucidate the interconnections between lipids metabolism, aging, and dietary composition, using DO-SR imaging the study visualized and quantified biomolecular metabolic activities in aging flies on different diets. Flies at 2, 10, 20, and 30 days old were fed foods containing 20% D_2O and different concentrations of sugar or protein (as in the lifespan test) for 5 days, then Raman spectra and SRS images of the fat body were collected (Fig. 3A, B). The lipid turnover rates, influenced by the varying diets, at each age were quantified. In flies on a standard diet (control), lipid turnover reduced with age (7-day to 35-day)

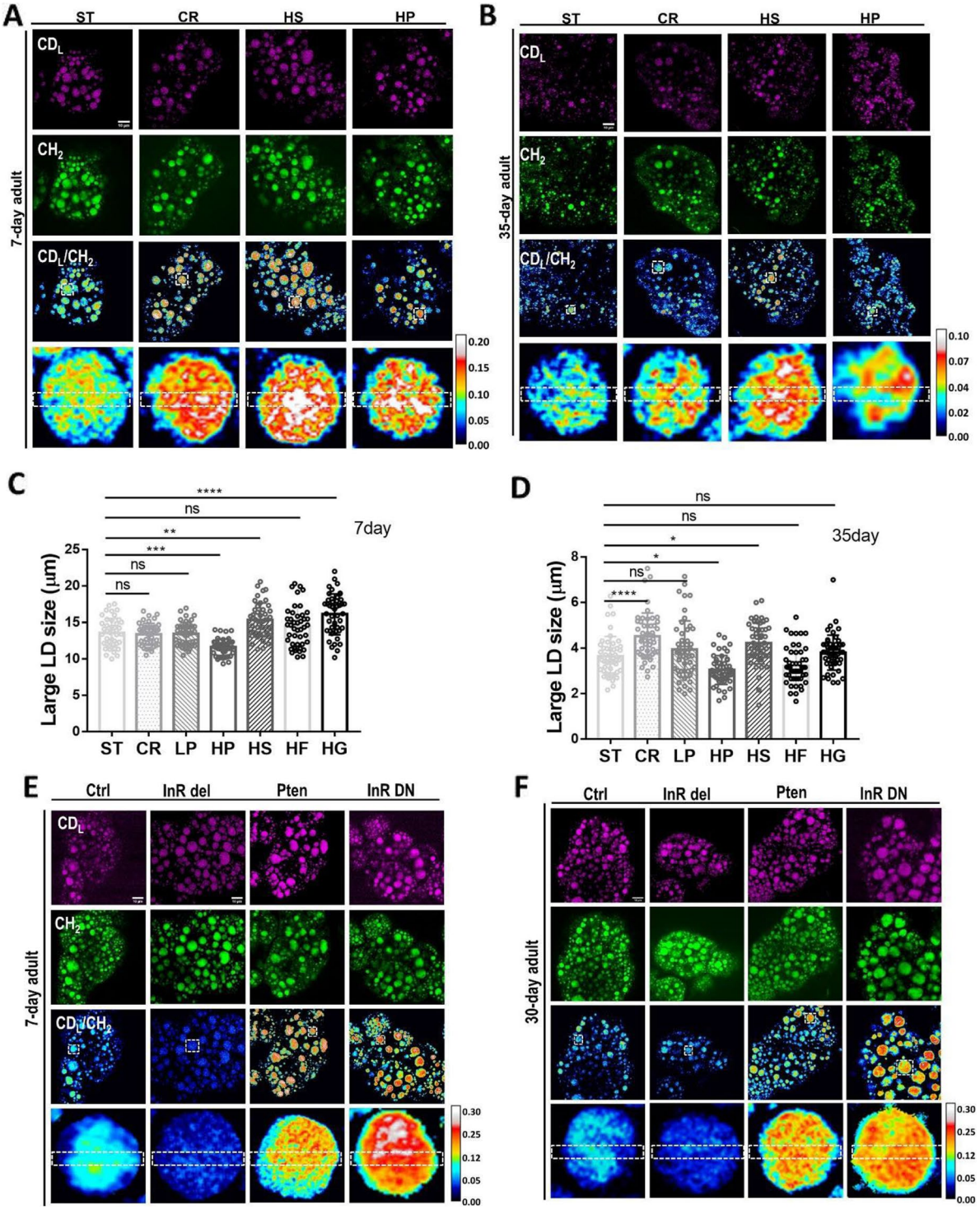

Fig. 3 DO-SRS imaging of diet-regulated lipid metabolic activity in young (**A**) and old (**B**) flies. The average sizes of large LDs were compared in young (**C**) and old (**D**) flies manipulated by diverse diets. ST, standard diet; CR, calorie restriction; LP, low protein; HP, high protein; HS, high sucrose; HF, high fructose; and HG, high glucose. Results are presented as Mean ± SD ($n = 50$, from 5 different individuals in each group). Statistical significance was determined by using one-way ANOVA. *, $p < 0.05$; **, $p < 0.01$; ***, $p < 0.001$; ****, $p < 0.0001$; ns, non-significant difference. Adapted from Li et al. (2022). **E**, **F** DO-SRS imaging of lipid metabolism in the fat body of mutant flies at (**E**) 7-day and (**F**) 30-day posteclosion. The ratiometric images (CD_L/CH_2) display the ratio of CD signal at 2143 cm^{-1} (newly synthesized lipids) to the signal at 2850 cm^{-1} (CH_2 stretching of lipids).The genetic downregulation of InR/PI3K pathway (Pten, ppl-Gal4 > UAS-Pten; InR DN, ppl-Gal4 > UAS-InRDN) showed higher lipid metabolism than control, and upregulation of InR/PI3K pathway (InR del, ppl-Gal4 > UAS-InR del) led to reduced lipid metabolism in both young and old flies. Adapted from reference (Li et al., 2022) [47]

significantly, which is consistent with previous observations [23]. High sucrose, high protein, and low protein diets as well as diets with a calorie restriction all reported increased lipid turnover when comparing flies at at 7 and 35 days old, but high fructose and high glucose diets only changed lipid turnover in 25- and 35-day-old flies. Different effects of glucose/fructose and sucrose on lipid metabolism suggest different mechanisms play a role, calorie may not be the only factor that regulates lipid metabolism, and monosaccharides and disaccharides are metabolized differently in the body, likely due to insulin resistance. Calorie restriction and low protein diets reduced insulin resistance and increased insulin sensitivity that stimulated more lipid synthesis [51]. High protein diet played the most significant role in enhancing lipid turnover at almost all ages; in addition, flies on a high protein diet reported a shortened lifespan. This is likely due to the insulinotropic effect of dietary protein, which increases insulin secretion, promotes lipid excretion, and slows lipid absorption and synthesis [52, 53], demonstrated by increased lipid turnover; but upregulation of the insulin signaling pathway shortened the lifespan [46].

To evaluate lipid catabolism along with the increased anabolism in flies on a high protein diet, starvation resistance was tested on flies on both a high protein diet and standard diet. After being treated with D_2O-labeled high protein and standard diets for 5 days, flies were given access to water but no food. Flies previously on high protein diet died within 48 h of starvation, while flies on standard food died in 120 h. This demonstrated that flies on high protein diets had a significantly increased lipid excretion that led to rapid death once on starvation. Quantitative measurements also determined flies on the high protein diet had a dramatically higher C-D turnover at 12 h of starvation compared with control, which drastically decreased at 24 h and 36 h, indicating increased lipid catabolism in flies on diets with high protein content.

Furthermore, spatiotemporal changes in LDs due to diet were examined. SRS imaging of LDs found that in both young and old flies, LD sizes were enlarged by high sugar diet but decreased dramatically by high protein diet (Fig. 3C, D). This further validated the role of high protein content diets in promoting lipid excretion and hindering lipid storage, which leading to the shrinkage in LDs and the reduction of total lipids thus led to enhanced lipid turnover. High sugar diets maintained or promoted lipid storage, displayed as changed LD size and increased lipid turnover due to increased lipid storage. Overall, old flies with longer lifespan, as regulated by high sugar and low protein diets, contained more large LDs as lipid storage, while old flies with more small LDs had a shorter lifespan.

DO-SRS imaging of lipid metabolic activities in aging fly mutants

The insulin/IGF-1 signaling (IIS) pathway plays an important role in regulating aging, as well as glucose and lipids homeostasis [54]. The phosphoinositide 3-kinase (PI3K) is a key molecule in the insulin signaling pathway. Inhibition of PI3K increased lipid metabolism in fly and mammalian adipose tissue, which led to lifespan extension via downregulating the IIS pathway [55].

Using DO-SRS imaging, metabolism in fly mutants were measured and quantified. A specific Gal4 driver in the fly fat body, *ppl-Gal4*, was used to drive *UAS-Pten* (a lipid phosphatase counteracting PI3K enzymatic activity) and *InR-DN* (the dominant-negative form of InR) expression, and *InR del* (the catalytic constitutive active form of InR) flies at ages of 2, 15, and 25 days that were fed D_2O-labeled standard food for 5 days. SRS imaging observed an evidently higher peak at 2143 cm^{-1} in *ppl-Gal4 > UAS-Pten* and *ppl-Gal4 > UAS-InRDN* flies, correspondingly, inhibiting (i.e. *Pten*) or inactivating (*InRDN*) the InR/PI3K signaling pathway significantly enhanced lipid turnover in flies at all ages, while upregulation (*InR del*) led to reduction of lipid metabolism. Furthermore, in each fly mutant during aging, downregulating InR/PI3K would maintain the high level of lipid metabolism, upregulating or inactivating of the pathway would lead to significant decline of lipid metabolism in older flies (Fig. 3E, F).

DO-SRS was further applied to assess the relative storages of saturated and unsaturated fatty acids in the fat body (with Raman peaks at 2880 and 3005 cm^{-1}, respectively). Unsaturated FAs were found to be dramatically reduced in all young fly mutants. Inhibiting the insulin pathway increased saturated FAs in fly mutants at all ages, and inactivating the pathway only promoted saturated FA storage in old flies, while upregulating the pathway reduced the storage in old flies.

This study demonstrates the capability of DO-SRS to directly visualize lipid metabolic activities in fruit fly when subjected to diet regulation, enhancing our understanding of the interconnections between lipid metabolism, aging, and nutrient-sensing pathway. Many more applications of this platform are envisioned in studying aging, diseases, and in much broader fields.

DO-SRS imaging of metabolic dynamics in aging Drosophila ovary

Above studies have set the criteria/workflow for using DO-SRS metabolic imaging in aging *Drosophila.* Thereafter, more studies were conducted on probing metabolic alterations in animal organs during development and aging,

including the ovary [56] and brain [57, 58]. This following study showcases the applications of SRS and DO-SRS microscopy in studying lipid and protein metabolic activities in female ovary during development and aging [56].

Temporal changes in stem cells have been found to contribute to aging and age-related diseases [59, 60]. Genetic and epigenetic pathways involved in stem cell maintenance, division, and differentiation are evolutionarily conserved. *Drosophila* ovary offers an ideal model system for studying stem cell aging [59, 61, 62]. Metabolic changes in the ovary impacts the quality of oocyte and the development of embryo. For example, dysregulation of protein homeostasis during aging is recognized as a causal factor of low-quality germ cells [63]. Nevertheless, how alterations in metabolism and specific chemical molecules influence ovary function during aging is still not fully understood, which is important for understanding the molecular mechanisms underlying premature ovarian failure and infertility diseases [64, 65].

Using DO-SRS imaging, metabolic activities of lipid and protein in ovarian follicles were studied during Drosophila development, and alterations of lipid profile in ovary was visualized during animal aging [56]. Flies at 0 and 30 days after eclosion were treated with 20% D_2O for 5 days for a stable and detectable incorporation of deuterium. Same as observed previously, C-D signal at 2140 cm^{-1} was from the newly-synthesized lipids and 2180 cm^{-1} newly-synthesized protein [23]. Evident C-D signals were detected in 5-day old flies at each development stage (germarium, stages 1, 3, 5, 8, and 14) of the ovarioles. Earlier developing stages of flies displayed higher protein synthesis, with no difference among different cell types. Lipid and protein synthesis in young ovary continuously increased with the germline development and reached the maximum level in mature oocytes. In 35-day the flies' lipid and protein syntheses were greatly reduced, indicating declined metabolism during aging in ovariole.

SRS imaging revealing different distributions of lipid subtypes in aging ovariole

To differentiate distinct spatial distributions of saturated and unsaturated lipids, SRS imaging at 2875, 3005, and 2852 cm^{-1} was performed, which corresponding to saturated, unsaturated, and total lipids, respectively [66–68]. SRS ratiometric images (divided by 2852 cm^{-1}) showed more saturated lipids localized in the germ stem cell niche of germarium in young (5-day old) females, but significantly decreased in old (35-day) flies (Fig. 4A, B).

Similarly, unsaturated lipids were also largely reduced in the germ stem cell niche in old flies, indicating the dramatic reductions of total lipids in this region during aging. However, in old flies, unsaturated lipids more accumulated in the germ cells (nurse cells and oocytes) but not in the surrounding follicle cells. They displayed a different distribution pattern of lipids compared to young flies, in which both saturated and unsaturated lipids were localized in the outer follicle cells and inside germ cells.

SRS imaging of protein distributions in aging ovary

A Raman peak at 1580 cm^{-1} was detected in the Raman spectrum, and it was determined to be either Cytochrome c or carotenoids. After treating the ovary with methanol that removed carotenoids, the peak remained, indicating it corresponded to Cytochrome c. This peak appeared in the germarium and at development stage 8 but not stage 14 in both young and old flies. Ratiometric images (divided by total protein at 2937 cm^{-1}) further displayed that in young flies' germarium Cytochrome c was localized within germ stem cell niche and the developing cysts, while in old flies the total level of Cytochrome c decreased, particularly in the germ stem cell niche (Fig. 4C). Cytochrome c was more evenly distributed in the cytoplasm of nurse and follicle cells in young ovary, but in old flies it was elevated in the nurse cells while reduced in the follicle cells.

DO-SRS imaging in aging Drosophila brain

Another recent study [57] utilizing DO-SRS imaging, alongside deuterated glucose and acetate, investigated lipid metabolism at the single organelle level in normal aging and mutant *Drosophila* to assess the effects of sex, diet, and genetic interventions on brain lipid metabolic dynamics.

The brain is the second-most lipid-rich organ after the adipose tissue [69]. It has been reported that in an aged brain, omega-3 fatty acids decline in concentration and lipid peroxidation levels increase [70, 71]. Additionally, dietary deficiency of omega-3 fatty acids may promote neurodegeneration [72], showing the crucial role lipid metabolism plays in brain function. Changes to lipid metabolism in the brain may also impact aging and lifespan [73]. Lipid droplets (LDs) in the brain are mainly localized in glial cells, where they play important roles in aging and neurodegeneration. LD in glial cells can protect polyunsaturated fatty acids in brain membranes from oxidation to maintain neural stem cell proliferation [74]. LD accumulation in microglia is involved in neurodegeneration [75], while inability to transfer lipids to glia for LD formation has been reported to lead to its acceleration [76]. However, how brain lipid metabolism is modulated during aging is not yet fully understood. Diet intervention affects aging process [49], but how diets regulate brain lipid metabolism remains elusive.

SRS imaging of lipid metabolism in aging brain

The study first collected Raman spectra of the brain, which displayed a significant reduction at the 2850 cm^{-1} (lipids)

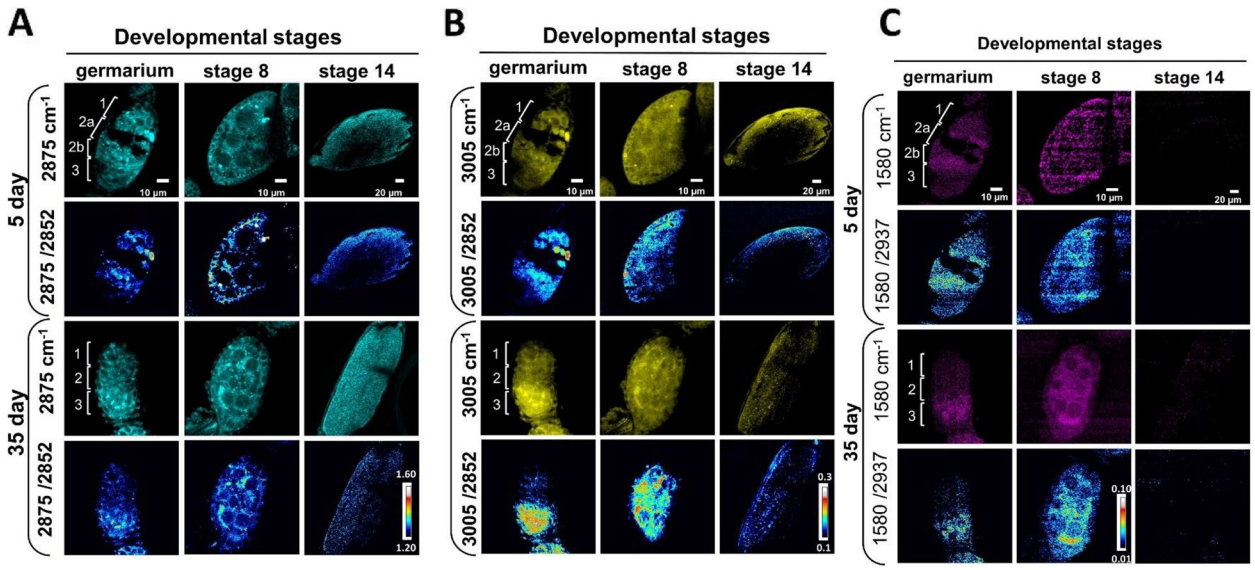

Fig. 4 SRS imaging of lipid subtype and Cytochrome c in aging Drosophila ovary. **A** SRS imaging at 2875 cm^{-1} of 5- and 35-day ovaries. Ratiometric images of 2875 cm^{-1}/2852 cm^{-1} were used to evaluate the concentration and distribution of saturated lipids. Higher saturated lipid content was shown in regions 1 and 2a of the germariums in young flies, but it was reduced in the germariums of 35-day old flies. Saturated lipids in region 2b were mainly localized in the lipid droplets inside the nurse cells of young flies, but they were condensed to the bar-shaped structures in old flies. At stage 8, saturated lipid was visualized in the cytoplasm of germ cells in both young and old files, but it was reduced in the surrounding follicle cells in old files. The level of saturated lipids at stage 14 was reduced in old flies compared with young ones. **B** SRS imaging at 3005 cm^{-1} of 5- and 35-day ovaries. The ratiometric images of 3005 cm^{-1}/2852 cm^{-1} were used to evaluate the concentration and distribution of unsaturated lipids. Unsaturated lipids were largely reduced in region 1 of the germarium during fly aging. However, they tended to be accumulated in region 3 in old flies, where germ cells were localized. The distribution of unsaturated lipids is consistent in repeated experiments for stage 8 follicles in old flies. Compared with the young flies, the content of unsaturated lipids in old files germ cells (nurse cells and oocytes) was increased, but it was reduced in the surrounding follicle cells (somatic cells). The level of unsaturated lipids at stage 14 was reduced in old flies compared with the young ones. **C** SRS imaging of Cytochrome c distribution in aging Drosophila ovary. SRS imaging at 1580 cm^{-1} in young and old ovaries. Ratiometric images of 1580 cm^{-1}/2937 cm^{-1} were used to evaluate the concentration and distribution of Cytochrome c. In day 5 germarium, Cytochrome c was detected in the germ stem cell niche and the developing cysts. However, in old flies, the overall level of Cytochrome c was decreased, especially in region 1 where germ stem cell niche was localized. At stage 8, Cytochrome c showed a clear mitochondrial pattern in the nurse cells in both young and old ovaries, which is consistent with its in situ localization to the intermembrane space of these organelles. In the young ovary, Cytochrome c was evenly distributed in the cytoplasm of nurse and follicle cells at stage 8, while its signal level was upregulated in the nurse cells and reduced in the follicle cells in old ovaries. Inside the nurse cells, Cytochrome c was more evenly distributed in young flies but more condensed in old flies. Scale bar, 10 μm in germarium and stage 8, and 20 μm stage 14. Adapted from reference (Li et al., 2021) [56]

peak in old (35-day) flies, which is consistent with SRS image results. Unsaturated lipids (at 1656 cm^{-1}) also displayed significant reduction in aged brain. Stimulated Raman histology (SRH) images were generated from protein (at 2930 cm^{-1}) and lipids (at 2850 cm^{-1}), which clearly displayed structural changes in old flies. Compared with young flies, old fly brains showed increased vacuoles-like structures, shape changes, and blurred boundaries in the neuropils. Lipid signals were mainly in the brain cortex region, which were from LDs. LD density was decreased but the size was enlarged with aging in both male and female flies. In particular, females had consistently higher LD density and more increase in LD size than males. These indicate that lipid metabolism changed in an age- and sex-dependent manner.

LD in aging *Drosophila* brain was next investigated. Using different key enzymes in triglyceride (TAG) synthesis and mobilized specifically in glia, the main contents of LDs was verified to be TAGs. Further, since lipid contents inside LDs can change greatly between cell types or even same type under different (age) contexts [77], which can be delineated by Raman spectral shape changes [78], SRS hyperspectral imaging of single LD was conducted on flies at different ages and sexes. There was no significant difference found between young and old brains, suggesting the content in LDs was not changed during aging.

DO-SRS imaging revealing brain lipid metabolic activities decreasing with aging

Remodeling of LD size is regulated by lipogenesis and lipolysis [45, 79]. To understand the underlying mechanism of brain LDs remodeling, this study used DO-SRS imaging to visualize lipid metabolic activity at single LD level

during fly aging. Flies at ages 0, 10, 20, 30, and 40 days were fed diets containing 20% D_2O for 5 days. LDs were imaged and lipid turnover was calculated by the ratio of CD signal (newly synthesized lipids, 2143 cm^{-1}) to CH signal (total lipids, 2850 cm^{-1}). Similar as in the fat body [47], newly synthesized lipids were observed to be non-uniformly distributed inside individual LDs. Quantification results showed that lipid turnover increased in young flies (5–15 days) to a peak at mid-age (15–35 days) before decreasing in old flies (35–45 days). Both females and males exhibited the same changing trend, but compared with males, females displayed earlier and more active lipid metabolism, which reached a maximum at an earlier stage (25 days vs. 35 days), and the turnover was consistently higher in young and mid-aged but lower in 45 days flies (Fig. 5A, B).

Interestingly, LD size in old flies was observed to be enlarged. Since the LD size is determined by lipogenesis and lipolysis, to probe which causes the enlarged LD in old flies, starvation assay was performed on 0- and 30-day flies. Flies were fed food containing 20% D_2O for 10 days first and then were deprived of food, after which lipid turnover was measured at 24, 48, and 72 h of starvation. The lipid turnover in LDs was found to decrease faster in young flies in both sexes, and faster in old males than females, indicating higher lipolytic rate in young flies than old flies, and higher in males than females. Thus, the enlarged LD size measured in old flies could be due to dramatic decline of lipolysis.

Diet restriction (DR) on lipid metabolism has been studied previously using DO-SRS in fly fat body [47]. Here, similar results were obtained, moreover, it was found that DR significantly enhanced lipid turnover in old (45-day) fly brain in both sexes, especially to a higher level in females. This implies DR hinders LD metabolism from becoming inert with aging. The LD size was also found to have been reduced under DR, but not the LD density.

DO-SRS imaging of lipid turnover regulation by IIS activity

The IIS pathway is a crucial regulator of development and aging [54]. Dysregulation of the IIS pathway would lead to insulin resistance, diabetes, and metabolic disorders [80, 81].

To understand the role of IIS plays in lipid metabolism in aging brain, imaging with DO-SRS was conducted on Drosophila mutants with reduced functional copies of *chico* (a homolog of insulin receptor substrate). The density and size of brain LDs were reduced significantly in both old female and male $chico^1/+$ flies, suggesting a decrease of lipid storage in the brain, which could be due to the enhanced lipid turnover. To verify this, DO-SRS imaging was used to measure lipid turnover dynamics in $chico^1/+$ mutant fly brain. Quantification results from DO-SRS showed remarkably increased lipid turnover in LDs of both young (7-day) and old (35-day) female $chico^1/+$ fly brains, but only slightly increased in males. This shows female flies had higher lipid turnover during aging, and reduction in IIS alter lipid metabolism plays different roles in females and males. The smaller LD size but larger lipid turnover in $chico^1/+$ flies suggests downregulation of IIS enhanced lipid exchanges between LD and membrane. This was further verified by using $dfoxo^{\Delta 94}$ and $dfoxo^{25}$ Drosophila mutants. LDs were greatly enlarged in *dfoxo* mutants especially in old flies, but no remarkable changes of lipid turnover in *dfoxo* females while significant reduction in males (Fig. 5C-I). Starvation assay indicated that these enlarged LDs were due to declined lipid mobilization during aging process.

Bioorthogonal SRS imaging revealing DR and IIS manipulation on metabolic shifts

Glia-specific IIS inhibition was shown to extend lifespan in *Drosophila* [82]. In addition to studies on the brain during development, Glial IIS regulation on lipid metabolic activities in the adult brain was investigated using SRS imaging in *Drosophila* mutants, including *GliaGS > UAS-Pten* (overexpressing *Pten*, a lipid phosphatase counteracting PI3K enzymatic activity), *GliaGS > UAS-InRDN* (dominant negative form of InR), and *GliaGS > UAS-lacZ* (control). It was found that both *UAS-Pten* and *UAS-InRDN* flies displayed reduced LD density in the brain. Next, DO-SRS imaging of lipid metabolic activities in 35-day flies mutants showed dramatically increased lipid turnover by downregulation of IIS activity in both *UAS-Pten* and *UAS-InRDN* females, but no significant change in males. Further, using neuron-specific *elavGS* driver to downregulate IIS did not change the LD density and lipid turnover, suggesting that neuronal IIS does not play a dominant role in brain lipid turnover. It is the glia-specific IIS that regulates brain lipid turnover.

Furthermore, to determine the metabolic origin of glial LDs, deuterated (D)-glucose and D-acetate were used for SRS imaging. Flies were fed diets containing D-glucose or D-acetate. SRS imaging found D-acetate derived lipids were increased in flies manipulated by DR and IIS downregulation, while D-glucose derived lipids were remarkably decreased subject to IIS downregulation. These findings indicated that brain metabolism using acetate is the major source for lipogenesis under DR or IIS downregulation.

DO-SRS imaging of lipid turnover in tauopathy brains

A latest study using Raman and DO-SRS imaging, studied lipid turnover in LDs accumulated in tauopathy brains.

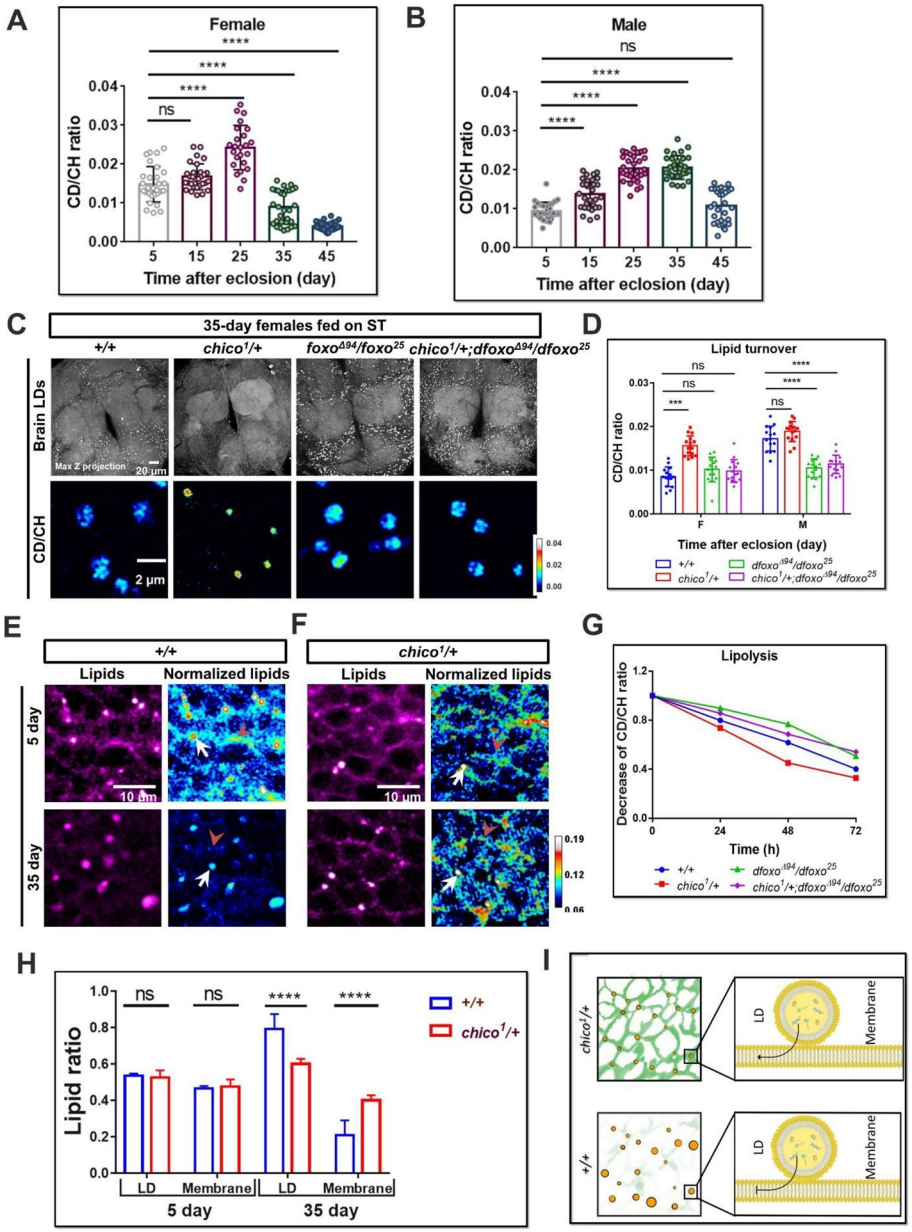

Fig. 5 DO-SRS imaging of metabolic activities in brain LDs during aging. **A**, **B** Quantification of CD/CH ratios in brain LDs from female (**A**) and male (**B**) flies. Brain LDs were imaged at 2143 cm^{-1} (CD, newly synthesized lipids) and 2850 cm^{-1} (CH, total lipids), respectively, and the ratios of newly synthesized lipids to total lipids (CD/CH) (lipid turnover) were quantified. Data are presented as mean ± SD. $n = 30$ ROIs from 8 brains, 3 technical repeats. Statistical significance was determined by using one-way ANOVA. ****$p < 0.0001$; ns, non-significant difference. **C**- **I** Lipid metabolic changes in IIS mutant flies. **C** Max Z projected images of the whole-mount brains (upper) and DO-SRS images of brain lipid turnover (lower) from IIS mutants (chico1/+, dfoxoD^{94}/dfoxo^{25} and chico1/+; dfoxoD^{94}/dfoxo^{25}) and control (w1118). **D** Quantification of lipid turnover rates in brain LDs from 7- (young) and 35-day (old) mutants. $n = 15$ ROIs from 3 to 5 brains. **E**, **F** The SRS images of 2850 cm^{-1} (magenta; left panels) demonstrate the subcellular distribution of lipids in cell body regions from young and old control flies (+/+) (**E**) and IIS mutants (chico1/+) (**F**). The ratiometric images of 2850 cm^{-1}/2930 cm^{-1} (royal; right panels) quantitatively map lipid levels in the membranes. White arrows, LDs; orange arrowheads, cell membranes. Scale bar: 10 μm. **G** The quantification LD lipid ratio (LD lipids/(LD lipids + membrane lipids)) and membrane lipid ratio (membrane lipids/(LD lipids + membrane lipids)) from (**E**) and (**F**). Data are presented as mean ± SD. **H** The time-course quantification of CD-lipid mobilization (CD/CH ratio decline) from brain LDs in 10-day IIS mutant flies after 0-, 24-, 48-, and 72-h starvation. Data are presented as mean ± SD. $n = 15$ ROIs from 3 to 5 brains at each group. **I** A model describing that the reduction in membrane lipids could be reversed by IIS downregulation. The membrane lipids were reduced during normal aging process but were preserved by chico1 mutant. Statistical significance was determined by using one-way ANOVA in (**D**), the statistical analysis in (**G**) was determined by using Student's t-test. ***$p < 0.001$; ****$p < 0.0001$; ns, non-significant difference. Adapted from reference (Li et al., 2023) [57]

Combining SRS imaging with genetic and pharmacological approaches, the study also assessed the role of neuronal AMPK pathway in LD metabolism, neuroinflammation and neuropathology in tauopathy brains [58].

LD has been recognized as signaling hubs for inflammation and immune response [83]. Disrupted or excessive LD accumulation is associated with metabolic diseases, infections, and neurodegeneration [84, 85]. Recent advances have linked LD to the pathophysiology of brain aging and neurodegenerative diseases [75, 86]. Astrocytes and microglia expressing ApoE4, the most known risk factor for developing AD, was found to accumulate cholesterol and lipids in LD [87–89]. To probe the molecular and cellular mechanisms of glial LD accumulation in AD brain, DO-SRS imaging and SRS imaging were employed to assess lipid turnover in LDs accumulated in tauopathy fly brain and induced pluripotent stem cell (iPSC) neurons, and lipids transfer from neurons to glia. The role of neuronal AMPK pathway in LD metabolism, neuroinflammation and neuropathology in tauopathy brain were also studied.

SRS imaging visualizing LDs accumulation in microglia of tauopathy brain

SRS imaging was used to visualize metabolism in wild type (WT) and P301S Tau transgenic (PS19) mouse brains. The P301S Tau exhibits the early symptoms of human tauopathy. Evident lipids signals (at 2850 cm^{-1}) were observed within LDs. Further, in the brain of both PS19 and WT mice at 2–3 months old, LDs were barely observed, but LD accumulation was remarkably higher in the hippocampus of 7–9 months PS19 mouse brain compared with WT mouse. Accompanying LD accumulation was the decrease of lipid signal in the membrane, while unsaturated lipid signal (at 3012 cm^{-1}) was observed enriched within LDs. All together, these suggest redistribution of unsaturated lipids from the membrane to LDs. Co-staining of the tissues with neuron- and glia-specific antibodies showed LDs were primarily accumulated in microglia (70%) and astrocytes (10%). 3D imaging in 9 months old PS19 mouse brain and co-registration with SRS lipid signal demonstrated the association of microglial LD accumulation with Tau pathology.

DO-SRS revealing tauopathy fly brain accumulating LDs with impaired lipid turnover

To study the metabolic dynamics in tauopathy brain, SRS imaging of *Drosophila* brains with pan-neuronal overexpression of human Tau (hTau), a tauopathy phenotype, found that more and larger LDs accumulated in the brains of 5-day hTau flies of both sexes than in control mice. These LDs were found to be mainly localized in the glia (Fig. 6).

Then DO-SRS imaging was performed to assess lipid turnover. Flies were fed foods containing 20% D_2O for 5 days and then subjected to 72-h starvation to assess the metabolism of D-labeled lipids. Right before the starvation assay, hTau flies displayed a higher lipid turnover (CD/CH signal ratio), i.e., greater lipogenesis in LDs. During the starvation, the CD/CH ratio decreased with time in both hTau and control flies, but in control flies the reduction was dramatic (by 58%) while hTau flies remained at a higher level, showing LDs in hTau fly brain had an inert lipid storage and compromised metabolic dynamics (Fig. 6).

DO-SRS revealing tauopathy neurons transfer lipids to glia

To visualize lipids distribution in tauopathy neurons, SRS imaging was performed in human iPSC-derived neurons homozygous for frontotemporal dementia (FTD)-causing V337M Tau mutation and healthy control (WT) neurons in vitro. Higher lipids signals in LDs and increased reactive oxygen species (ROS) levels were observed in V337M neurons, and the LDs were enriched with unsaturated lipids. Next, lipid turnover in these two cell lines were observed using DO-SRS. It was shown that V337M neurons displayed a higher CD/CH ratio in LDs, showing a higher level of lipogenesis. During wash-off, CD/CH ratio decreased steadily to zero in WT neurons, while decreasing much slower in V337M and still maintaining a high level after 72 h of starvation, indicating less active lipid turnover. Together, these findings demonstrated that tauopathy neurons accumulated LDs due to increased lipogenesis and reduced lipid mobilization.

To investigate if LDs were transferred from tauopathy neurons to microglia, DO-SRS imaging was conducted on a media transfer experiment, in which neuronal conditioned media (NCM) from 5-week-old iPSC neurons was transferred to mouse microglia to replace 50% of glial media. Strong lipid SRS signal (in LD) was detected in BV2 cells treated with NCM transferred from iPSC neurons, but not those treated with WT-NCM (control). DO-SRS imaging further revealed more D-labeled LDs in V337M-NCM treated but not control neurons. All together, these demonstrated a lipid transfer mechanism that tauopathy neurons transferred lipids to glia and induced LD accumulation in glia.

Overexpression of neuronal AMPK inhibits LD accumulation in tauopathy brain

Neuronal AMP-activated protein kinase (AMPK) has been shown to play a critical role in regulating lipid metabolism [90, 91]. Measuring AMPK activity by immunoblot in the cortical lysates of 9 months PS19 mice showed decreased phosphorylated AMPK, indicating impaired AMPK activity in tauopathy brains. Next, how AMPK activity affects

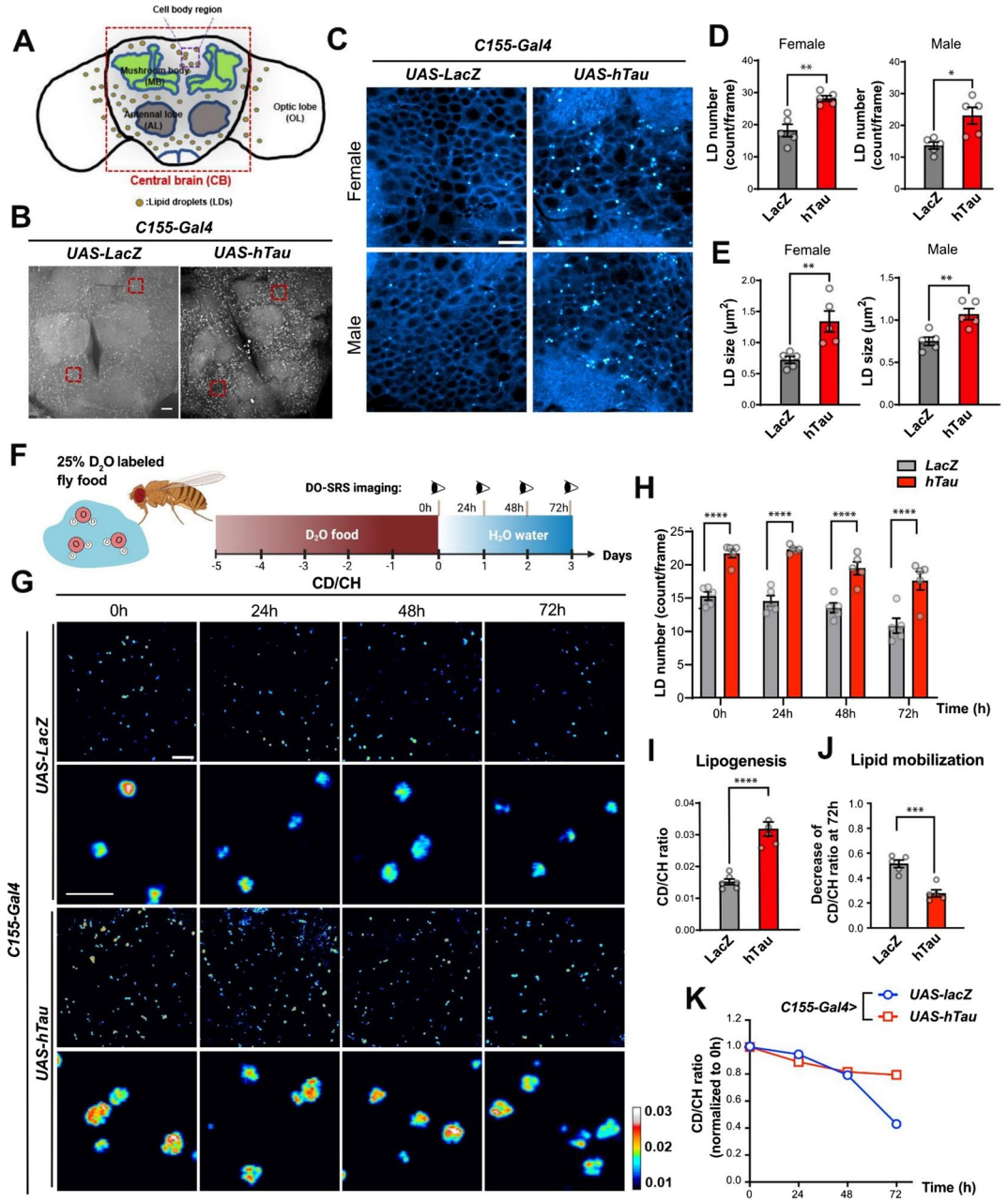

Fig. 6 LDs accumulate in human Tau (hTau) overexpressing Drosophila brains and have slower lipid turnover. **A** A cartoon depicts the structure of Drosophila adult brain. CB, central brain; OL, optical lobe. Neuropils (mainly mushroom bodies [MBs] and antenna lobes [ALs]) are surrounded by cortical regions where LDs (yellow dots) are primarily localized. **B** Max Z-projected SRS images of hemibrain (red box in A) from hTau flies (elavC155-Gal4 > UAS-hTau) and control flies (elavC155-Gal4 > UAS-lacZ). Scale bars: 20 μm. **C** Zoomed-in SRS images showing that LDs primarily localize to the cortical regions (red boxes in B) of control and hTau fly brains of both sexes. Scale bars: 10 μm. **D** and **E** Quantification of LD number (**D**) and size (**E**) in female and male brains of hTau flies compared with control flies. **F** A schematic of DO-SRS imaging paradigm to assess lipid metabolic dynamics in fly brains. Flies were fed D_2O food for 5 days, then transferred to a tube containing a H_2O-moistened filter paper and subjected to starvation for 3 days. DO-SRS imaging was done at 0, 24, 48, and 72 h after media change. **G** DO-SRS images of CD/CH ratio at 0, 24, 48, and 72 h starvation in control and hTau fly brains. Scale bars: 10 μm in zoomed-out images, 5 μm in zoomed-in images. **H** Quantification of LD number in WT and hTau fly brains during starvation after D_2O labeling. **I** Quantification of lipogenesis in brain LDs after D_2O labeling by CD/CH ratio at 0 h. **J** Quantification of lipid mobilization (the decrease in CD/CH ratio) of brain LDs at 72 h starvation. **K** Change of CD/CH ratio within brain LDs at each time point during starvation, normalized to 0 h. **D**, **E**, **H**, **I**, **J**, and **K**) $n = 5$ fly brains per group. **D**, **E**, **H**, **I**, and **J** Values are mean ± SEM. (K) Values are mean ± SD. * $p < 0.05$; ** $p < 0.01$; *** $p < 0.001$; **** $p < 0.0001$, by Student's t-test. Adapted from reference (Li et al., 2024) [58]

LD accumulation was investigated. DO-SRS imaging was performed in AICAR-treated V337M iPSC neurons. After 5 days of D_2O labeling, AICAR was added to water media during 72-h wash-off period. LD number was found to decrease at 48- and 72-h and a lower CD/CH ratio in LDs was also measured, indicating enhanced lipids mobilization that was activated by AMPK (Fig. 7A-D).

Then regulation of neuronal AMPK on LD accumulation was assessed. Overexpression of AMPK was found to reduce the number and size of LDs in the brain of female hTau flies but not in WT flies. Previous study showed AMPK activation was induced by starvation [92]. An increase of AMPK activity was also detected in WT flies on starvation, but not in hTau flies on starvation. Further, how starvation impacts LD dynamics in hTau fly brain was examined using DO-SRS imaging. Overexpression of neuronal $AMPK^{WT}$ was found to lead to decreased LD number, accompanied by declined lipogenesis and accelerated lipid turnover in LDs in hTau fly brains during 72-h starvation, as measured by CD/CH ratios.

Inhibition of neuronal AMPK exacerbating LD accumulation and neuroinflammation in mice

Influence of neuronal AMPK on LD accumulation in tauopathy mouse brain was also examined. SRS imaging and RT-qPCR analyses showed that in AMPK depletion (and reduced AMPK activity) mouse mutants, LD accumulation was significantly increased. Increased levels of cleaved caspase-1 were also observed in the hemihippocampi of mouse mutants, showing increased apoptosis and inflammasome activation. Further, LDs were found to be densely localized in the neuronal layers, suggesting potential involvement of LDs in neuronal inflammasome activation at an early stage of tauopathy (Fig. 7E-K).

DO-SRS imaging of metabolic activities in breast cancer

In addition to aging and aging-related disease, recent studies have employed DO-SRS imaging, integrated with two photon microscopy, on triple negative breast cancer (TNBC) cells and tissues [93, 94].

DO-SRS imaging of metabolic activities for distinguishing TNBC subtypes

A core hallmark of cancer is deregulated cellular metabolism [95]. Lipid metabolism is involved in many cellular processes such as cell growth, proliferation, differentiation, membrane homeostasis, and energy maintenance. In cancer, lipid metabolism is highly reprogrammed, such as increased lipogenesis and uptake, and increased lipid turnover from intracellular LD [96, 97]. Triple negative breast cancer (TNBC) is a highly aggressive cancer with a poor prognosis and high incidence of metastasis [98]. TNBC has six subtypes including basal-like 1 (BL1), basal-like 2 (BL2), immunomodulatory (IM), mesenchymal-like (M), mesenchymal stem-like (MSL), and luminal androgen receptor (LAR). Each subtype displays varying responses to targeted treatment [99]. Early detection of TNBC and distinguishing its subtypes are crucial for disease prognosis and treatment.

In the study [93], TNBC cell lines from different subtypes and non-TNBC cells were xenografted to mouse mammary fat pad, including HCC70 (BL2), HCC1806 (BL2), MDA-MB468 (BL1) and MDA-MB231 (MSL), as well as BT474 (non-TNBC). After tumors reached volumes ~ 100 – 110 mm^3 (except ~ 260 mm^3 for HCC1806), mice were fed drinking water containing 25% D_2O for 8 days. Breast cancer tissues were then excised for imaging. Multimodal imaging was performed to analyze distinct biomolecules within the same region of interest (ROI) in each tissue sample. Two photon fluorescence (TPF) microscopy was used to image FAD and NADH, subsequently, second harmonic generation (SHG) imaging was applied to visualize collagen fibers, and then DO-SRS imaging was employed to investigate lipid and protein metabolic activities.

DO-SRS imaging characterizing lipids and protein metabolism in tumor tissues

DO-Raman was used to collect Raman spectra of the extracellular matrix (ECM) for identifying characteristic peaks. The spectra showed that TNBC subtype BL2 (HCC1806) had the highest intensity at 2186 cm^{-1}, corresponding to newly-synthesized protein, while non-TNBC tissue had the lowest intensity, indicating enhanced protein metabolism in TNBC.

To probe lipogenesis, protein in the tissue samples was removed by proteinase K treatment. DO-SRS ratiometric images of newly-synthesized lipids (CD_L at 2130 cm^{-1}) to total lipid (CH_L at 2850 cm^{-1}) showed significantly higher lipid turnover in MSL tissues (MDA-MB231) than other subtypes and non-TNBC (BT474) tissues. While there was no substantial difference between TNBC subtypes and BT474 tissues. This result suggested that lipid turnover could be severed as a biomarker to distinguish subtype MSL from other subtypes (Fig. 8A-D).

Subsequently, to examine de novo protein synthesis, lipids in the tissues were removed by methanol wash. DO-SRS ratiometric images of newly-synthesized protein (CD_p at 2180 cm^{-1}) to total protein (CH_p at 2930 cm^{-1}) displayed

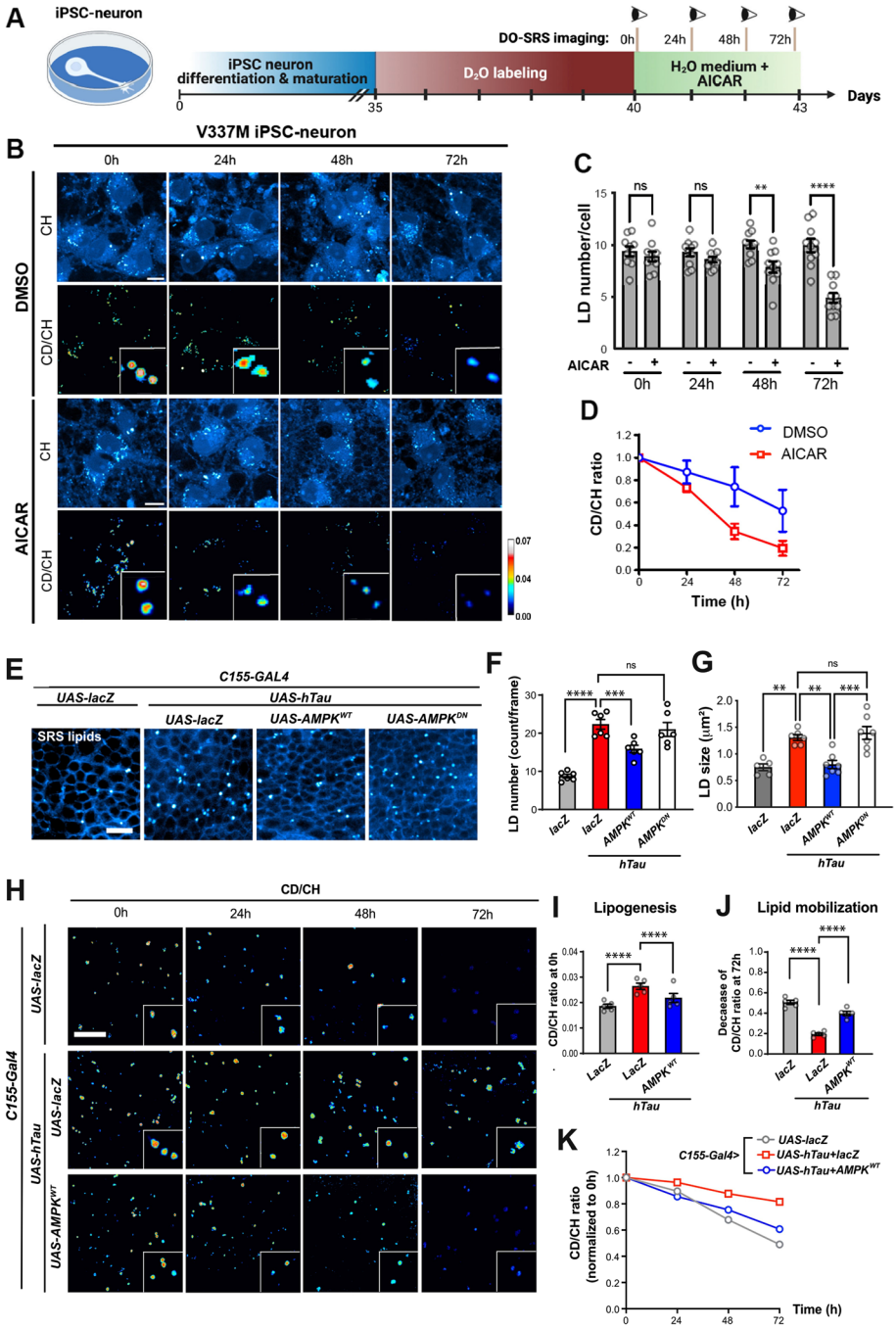

Fig. 7 **A**-**D** AMPK inhibits LD accumulation, promotes lipid turnover in neurons, and decreases neuronal-media-induced LD accumulation in microglia. **A** A schematic of DO-SRS imaging timeline in AICAR-treated V337M iPSC neurons. 5-week-old iPSC neurons were cultured in 50% D_2O neuronal media for 5 days, followed by complete media change to H_2O media containing AICAR (250 mM) for 3 days. **B** DO-SRS images showing CD/CH ratio in V337M iPSC neurons at 0, 24, 48, and 72 h in H_2O media with DMSO or AICAR treatment. Scale bars: 10 μm. **C** and **D** Quantification of LD number (**C**) and CD/CH ratio (**D**) in V337M iPSC neurons with DMSO or AICAR treatment in H_2O media. $n = 10$ ROIs from 3 independent experiments. **E**-**K** Neuronal AMPK negatively regulates LD accumulation in tauopathy fly and mouse brains. (**E**) Representative SRS images showing brain LDs from female WT flies (elavC155-al4 > lacZ), hTau flies (elavC155-Gal4 > hTau; lacZ), and hTau flies with neuronal overexpression of AMPK (elavC155-Gal4 > hTau; AMPKWT, elavC155-Gal4 > hTau; AMPKDN). Scale bars: 10 μm. **F** and **G** Quantification of LD numbers (**B**) and size (**C**) in (**A**). $n = 6$–7 fly brains per group. **H** DO-SRS images of CD/CH ratio after 0, 24, 48, and 72 h of starvation in female control and hTau fly brains with or without AMPKWT overexpression. Scale bars: 10 μm. **I**–**K** Quantification of lipogenesis by CD/CH ratio at 0 h (**I**); lipid mobilization by the decrease of CD/CH ratio within LDs at 72 h (**J**); and changes in CD/CH ratio at 0, 24, 48, and 72 h starvation, normalized to CD/CH ratio at 0 h (**K**). $n = 5$ fly brains per group. Adapted from reference (Li et al., 2024) [58]

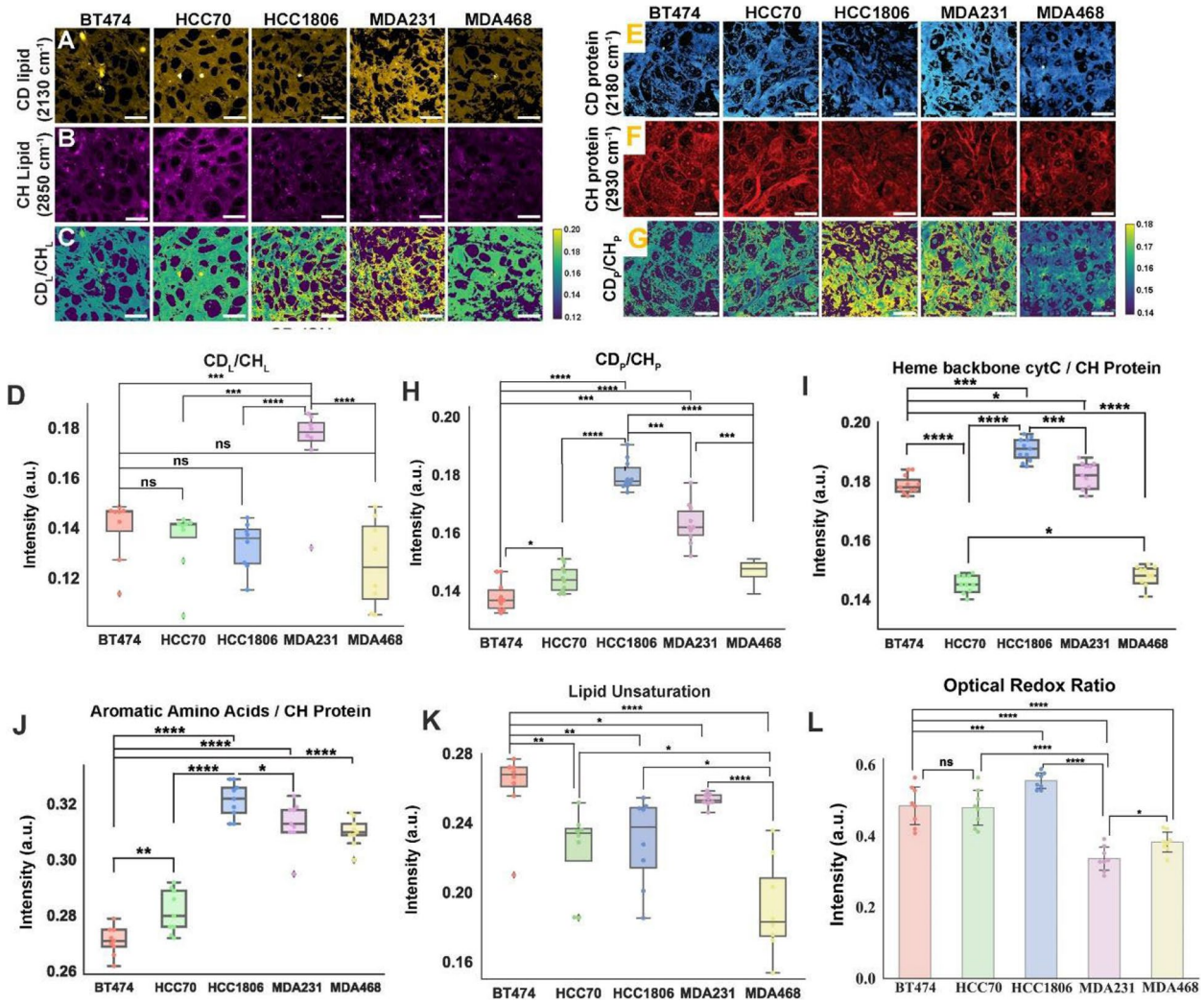

Fig. 8 DO-SRS imaging of lipid and protein metabolic activities in TNBC tissues. **A**, **B** SRS images of newly synthesized and total lipid distribution in different types of tumors, respectively. These samples are treated with proteinase K, which breaks down proteins to reveal clearer lipid signal. **C** Ratiometric images of CD_L/CH_L in tissues. **D** Quantification of lipid turnover rate. There was a significantly higher lipid turnover rate in MDA-MB231 tissue compared with other subtypes. Statistical significance was determined by using one-way ANOVA test. ***, $p < 0.001$; ****, $p < 0.0001$. Scale bar: 20 μm. **E**, **F** SRS images illustrated the newly synthesized and total protein distribution in TNBC tissues, respectively. These samples were treated with methanol, which eliminated lipids to reveal clearer protein signal. **G** Ratiometric images of CD_P/CH_P. **H** Quantification of protein turnover rate. HCC1806 tissue had significantly high protein turnover and non-TNBC tissue (BT-474) had the lowest. Statistical significance was determined by using one-way ANOVA test. *, $p < 0.05$; ***, $p < 0.001$; ****, $p < 0.0001$. Scale bar: 20 μm. **I**, **J** Quantitative results of ratiometric images showed significantly higher cytochrome c and AAA in HCC1806 and MDA-MB231 tissues. **K** Quantification of unsaturated lipid in different tissues. **L** Quantification of optical redox ratio. In MDA-MB231 tissues, the optical redox ratio was significantly lower than in all other tissues. Statistical significance was determined by using one-way ANOVA test. *, $p < 0.05$; **, $p < 0.01$; ***, $p < 0.001$; ****, $p < 0.0001$. Adapted from reference (Li et al., 2023) [93]

the highest protein turnover in HCC1806 (subtype BL2) tissues, followed by MDA-MB231 (subtype MSL) tissues. All TNBC tissues showed considerably higher protein turnover than non-TNBC tissue (Fig. 8E-H). Therefore, protein turnover can be used to distinguish MSL and BL2 subtypes from other subtypes, and to discriminate HCC1806 from HCC70 even within same BL2 subtype.

SRS imaging for mapping protein and unsaturated lipids

Raman imaging was also used to map cytochrome c distribution in TNBC tissue, in addition to Drosophila ovary during aging. SRS images for cytochrome c were acquired at 1580 cm^{-1} and compared with the total protein at 2930 cm^{-1}. Ratiometric images and quantification results

showed higher levels of cytochrome c in HCC1806 (subtype BL2) tissues, followed by MDA-MB231 (subtype MSL) and BT474 (non-TNBC) tissues, while HCC70 tissues displayed the lowest level (Fig. 8I).

Aromatic amino acids (AAAs), including phenylalanine, tyrosine, and tryptophan, play an important role in the stabilization of overall structure of protein, and cancerous breast tissues exhibited overexpression of AAA [100]. A previous study used DO-SRS imaging to investigate metabolic changes under excess AAA in cancer cells, and found decreased protein synthesis in cells, indicating elevated oxidative stress and dysfunction of mitochondria [101]. Here, ratiometric images of AAA (at 3063 cm^{-1}) to total protein (2930 cm^{-1}) demonstrated that AAA contents in all TNBC tissues were significantly higher than that in non-TNBC tissue, while HCC1806 had the highest and HCC70 had the lowest content among TNBC tissues (Fig. 8J).

Unsaturated lipids have previously been shown to inhibit breast cancer proliferation and differentiation [102]. Therefore, contents and distributions of unsaturated lipids in TNBC tissues were examined using SRS imaging. Ratiometric images of unsaturated lipids (at 3011 cm^{-1}) to total lipids at 2880 cm^{-1} revealed significantly higher unsaturated lipids in non-TNBC (BT474) tissue compared with all TNBC tissues. Among TNBC tissues, MDA-MB468 (subtype BL1) had the lowest contents of unsaturated lipids (Fig. 8K).

Optical redox ratio and collagen fiber morphology in TNBC tissues

The SRS microscopy was integrated with TPF and SHG for multimodal imaging. NADH and FAD play crucial roles in cellular metabolism. The optical redox ratio, defined as FAD / (FAD + NADH), reflects the level of cellular metabolism and mitochondrial activities. Here, autofluorescence imaging of NADH and FAD was conducted using TPF. The quantified redox ratio was significantly different in non-TNBC BT474 tissues compared with TNBC tissues, except HCC70. Among all TNBC tissues, MDA-MB231 (MSL) tissues showed the lowest value (Fig. 8L).

Collagen fibers play a crucial role in ECM. They have significant impact on morphogenesis and tumor progression [103]. SHG imaging was hence employed for studying collagen fiber morphology in TNBC tissues. Collagen fibers in TNBC tissues were found to be less curved compared with non-TNBC tissue, especially near the boundary of tumor. Fiber angles and anisotropy were also evaluated. All TNBC tissues exhibited significantly higher anisotropy than non-TNBC tissue, and the anisotropy was evidently higher at the boundary than the center in all TNBC tissues. These indicate that TNBC tissues' more aggressive feature and rapid progression at the boundary.

Insulin and methionine interplay in TNBC cellular metabolism

A hallmark of TNBC is its hyperactivity of mTOR pathways, which play crucial roles in glucose, lipid, and protein metabolism. Insulin and methionine have been shown to be involved in mTOR pathways [104, 105], and directly affect proliferation in TNBC [106–108].

To better understand the interplay between methionine, insulin, and subcellular metabolism in TNBC cells, DO-SRS imaging was applied to examine lipid metabolic dynamics inside TNBC cells [94]. TNBC cells (MDA-MB231) and normal breast epithelial cells (MCF10A) were cultured with 20 × methionine in the growth media supplemented with 50% D_2O. Various concentrations of insulin (01x, 1x, and 2x) were then added to the media. MCF10 cells exhibited decreased lipid/protein ratio with addition of excess methionine, while in TNBC cells the ratio significantly increased with excess methionine with addition of 1 × and 2 × insulin. DO-SRS imaging was then performed to examine newly-synthesized lipid and protein. Combining CD_L/CH_L and CD_L/CD_P ratios, it was shown that excess methionine promoted de novo lipogenesis in both cell lines. Next, the morphological changes in LDs were assessed by leveraging 3D SRS imaging. It was observed that LD number was reduced but volume was increased under excess methionine in both cells. Of note is the insulin restricted case (0.1 x) in TNBC, the changes measured were insignificant quantitatively. Finally, lipid peroxidation status in both cell lines was analyzed by using TPF. It was found that TNBC was more heavily influenced by methionine concentration. In MCF10A cells, de novo synthesis of chain fatty acids was upregulated by excess insulin concentration, but excess insulin did not influence peroxidation in TNBC as much as methionine.

Conclusions and outlook

Since the first application of SRS microscopy for bioimaging [6], extensive applications of SRS microscopy have been carried out for metabolic imaging in life science. SRS displays many advantages including high sensitivity, high chemical specificity, high spatial resolution (subcellular), imaging speed 1000 times faster than spontaneous Raman, and signal linearly proportion to molecule's concentration. Employing vibrational tags for SRS imaging enables visualization of small biomolecules metabolism in live cells and organisms. Particularly, D_2O is shown as a universal probe to visualize and track metabolic dynamics of various biomolecules simultaneously — improving upon deuterium probes, which can only track a particular biomolecule. The application of deuterium-labeled probes is not solely limited to *Drosophila* or cellular models, bur has also been

applied to a variety of different animal models. Deuterated molecules have been readily utilized in mice; from the study of AMPK regulation in tauopathy mouse brains [58] to measuring protein synthesis through carotid injection of deuterated amino acids [18] to quantifying glucose metabolism via [D_7]-glucose administration [22]. Furthermore, lipid and protein synthesis in both *C. elegans* larvae and zebrafish embryos have been imaged following D_2O treatment [16].We envision DO-Raman and DO-SRS imaging can even be implemented in human studies with low heavy water dosage in the near future, enhancing the essential roles this technology will play in studying aging and age-related diseases.

Aside from metabolic vibrational probing, developments toward enhancing imaging resolution and depth are plausible. SRS has the same diffraction-limited resolution as found in the two-photon microscopy. To improve the resolution, shorter wavelength laser source may be employed, but it is still limited by diffraction. Efforts have been made on instrumentation [109, 110], Raman probe [111], and data processing techniques for super resolution SRS imaging beyond the diffraction limit. A recent study developed a deconvolution algorithm, adaptive moment estimation (Adam) optimization-based pointillism deconvolution (A-PoD), for SRS imaging and achieved super-resolved images (up to 59 nm) in cells and tissues of mammalian and Drosophila [112]. This imaging processing approach allows for quantitatively measuring nanoscopic colocalization of biomolecules and metabolic dynamics in organelles, which reveals broad applications in other imaging modalities besides SRS. Increasing imaging depth is also a challenge for metabolic imaging, which is influenced by the scattering and absorption of biological samples. Tissue clearing method may be adopted to facilitate imaging, such as utilized in recent study that employing urea and Triton to enhance imaging depth 10-fold [113].

Although Raman/SRS, as one single imaging modality, displays many advantages, it can only provide limited information from a specific perspective. More and more studies have combined Raman imaging with other optical imaging modalities including TPF, SHG, fluorescence lifetime imaging microscopy (FLIM), Optical Coherence Tomography (OCT), and Fourier Transform Infrared (FTIR), for bioimaging in translation research [114–118]. Multimodal imaging modalities allow researchers to assess different biomarkers within a biological sample from different aspects, to improve diagnostic accuracy and reliability. For example, using a multimodal imaging system, incorporating SRS, TPF, and SHG, we distinguished TNBC subtypes based on lipid/protein metabolism, optical redox ratio, and collagen fiber anisotropy [93]. We believe multimodal imaging modalities will evolve rapidly and become essential tools in both research and clinics in the near future, while Raman/SRS will keep playing a key role in metabolic imaging.

Acknowledgements We wish to acknowledge the contributions of the original authors of the innovative studies reviewed above.

Authors' contributions LS initiated the idea of the study. LS and JV collected and reviewed the studies that significantly contributed to the outline of the review paper and drafted the manuscript. All authors approved the final submission of this review paper.

Funding This work was supported by NIH grants R01NS111039, R01 GM149976, 5R01NS111039, and R21NS125395. U54CA132378, U54DK134301, and U54-HL165443. Additional support was provided by the start-up fund from UC San Diego Jacob School of Engineering.

Data availability Not applicable.

Declarations

Competing interests The author declares no competing interests.

References

1. Skala MC, et al. In vivo multiphoton microscopy of NADH and FAD redox states, fluorescence lifetimes, and cellular morphology in precancerous epithelia. Proc Natl Acad Sci U S A. 2007;104:19494–9. https://doi.org/10.1073/pnas.0708425104.
2. Yu Q, Heikal AA. Two-photon autofluorescence dynamics imaging reveals sensitivity of intracellular NADH concentration and conformation to cell physiology at the single-cell level. J Photochem Photobiol B. 2009;95:46–57. https://doi.org/10.1016/j.jphotobiol.2008.12.010.
3. Stringari C, et al. Multicolor two-photon imaging of endogenous fluorophores in living tissues by wavelength mixing. Sci Rep. 2017;7:3792. https://doi.org/10.1038/s41598-017-03359-8.
4. Cheng JX, Jia YK, Zheng G, Xie XS. Laser-scanning coherent anti-Stokes Raman scattering microscopy and applications to cell biology. Biophys J. 2002;83:502–9. https://doi.org/10.1016/S0006-3495(02)75186-2.
5. Evans CL, et al. Chemical imaging of tissue in vivo with video-rate coherent anti-Stokes Raman scattering microscopy. Proc Natl Acad Sci U S A. 2005;102:16807–12. https://doi.org/10.1073/pnas.0508282102.
6. Freudiger CW, et al. Label-free biomedical imaging with high sensitivity by stimulated Raman scattering microscopy. Science. 2008;322:1857–61. https://doi.org/10.1126/science.1165758.
7. Shaw RA, Kotowich S, Leroux M, Mantsch HH. Multianalyte serum analysis using mid-infrared spectroscopy. Ann Clin

Biochem. 1998;35(Pt 5):624–32. https://doi.org/10.1177/000456329803500505.
8. Shaw RA, Kotowich S, Mantsch HH, Leroux M. Quantitation of protein, creatinine, and urea in urine by near-infrared spectroscopy. Clin Biochem. 1996;29:11–9. https://doi.org/10.1016/0009-9120(95)02011-x.
9. Min W, Freudiger CW, Lu S, Xie XS. Coherent nonlinear optical imaging: beyond fluorescence microscopy. Annu Rev Phys Chem. 2011;62:507–30. https://doi.org/10.1146/annurev.physchem.012809.103512.
10. Hu F, Shi L, Min W. Biological imaging of chemical bonds by stimulated Raman scattering microscopy. Nat Methods. 2019;16:830–42. https://doi.org/10.1038/s41592-019-0538-0.
11. Cheng JX, Xie XS. Vibrational spectroscopic imaging of living systems: An emerging platform for biology and medicine. Science. 2015;350:aaa8870. https://doi.org/10.1126/science.aaa8870.
12. Shen Y, Hu F, Min W. Raman Imaging of Small Biomolecules. Annu Rev Biophys. 2019;48:347–69. https://doi.org/10.1146/annurev-biophys-052118-115500.
13. Jones RR, Hooper DC, Zhang L, Wolverson D, Valev VK. Raman techniques: fundamentals and frontiers. Nanoscale Res Lett. 2019;14:231. https://doi.org/10.1186/s11671-019-3039-2.
14. Fung AA, Shi L. Mammalian cell and tissue imaging using Raman and coherent Raman microscopy. Wiley Interdiscip Rev Syst Biol Med. 2020;12: e1501. https://doi.org/10.1002/wsbm.1501.
15. Zhao Z, Shen Y, Hu F, Min W. Applications of vibrational tags in biological imaging by Raman microscopy. Analyst. 2017;142:4018–29. https://doi.org/10.1039/c7an01001j.
16. Shi L, et al. Optical imaging of metabolic dynamics in animals. Nat Commun. 2018;9:2995. https://doi.org/10.1038/s41467-018-05401-3.
17. Wei L, et al. Imaging complex protein metabolism in live organisms by stimulated Raman scattering microscopy with isotope labeling. ACS Chem Biol. 2015;10:901–8. https://doi.org/10.1021/cb500787b.
18. Shi L, Shen Y, Min W. Invited Article: Visualizing protein synthesis in mice with in vivo labeling of deuterated amino acids using vibrational imaging. APL Photonics. 2018;3. https://doi.org/10.1063/1.5028134.
19. Yu Y, Mutlu AS, Liu H, Wang MC. High-throughput screens using photo-highlighting discover BMP signaling in mitochondrial lipid oxidation. Nat Commun. 2017;8:865. https://doi.org/10.1038/s41467-017-00944-3.
20. Alfonso-Garcia A, Pfisterer SG, Riezman H, Ikonen E, Potma EO. D38-cholesterol as a Raman active probe for imaging intracellular cholesterol storage. J Biomed Opt. 2016;21:61003. https://doi.org/10.1117/1.JBO.21.6.061003.
21. Hu F, Wei L, Zheng C, Shen Y, Min W. Live-cell vibrational imaging of choline metabolites by stimulated Raman scattering coupled with isotope-based metabolic labeling. Analyst. 2014;139:2312–7. https://doi.org/10.1039/c3an02281a.
22. Zhang L, et al. Spectral tracing of deuterium for imaging glucose metabolism. Nat Biomed Eng. 2019;3:402–13. https://doi.org/10.1038/s41551-019-0393-4.
23. Li Y, Zhang W, Fung AA, Shi L. DO-SRS imaging of metabolic dynamics in aging Drosophila. Analyst. 2021;146:7510–9. https://doi.org/10.1039/d1an01638e.
24. Yue S, Cheng JX. Deciphering single cell metabolism by coherent Raman scattering microscopy. Curr Opin Chem Biol. 2016;33:46–57. https://doi.org/10.1016/j.cbpa.2016.05.016.
25. Lee HJ, Cheng JX. Imaging chemistry inside living cells by stimulated Raman scattering microscopy. Methods. 2017;128:119–28. https://doi.org/10.1016/j.ymeth.2017.07.020.
26. Hill AH, Fu D. Cellular imaging using stimulated raman scattering microscopy. Anal Chem. 2019;91:9333–42. https://doi.org/10.1021/acs.analchem.9b02095.
27. Shi L, Fung AA, Zhou A. Advances in stimulated Raman scattering imaging for tissues and animals. Quant Imaging Med Surg. 2021;11:1078–101. https://doi.org/10.21037/qims-20-712.
28. Kumamoto Y, Harada Y, Takamatsu T, Tanaka H. Label-free molecular imaging and analysis by raman spectroscopy. Acta Histochem Cytochem. 2018;51:101–10. https://doi.org/10.1267/ahc.18019.
29. Krafft C, Schie IW, Meyer T, Schmitt M, Popp J. Developments in spontaneous and coherent Raman scattering microscopic imaging for biomedical applications. Chem Soc Rev. 2016;45:1819–49. https://doi.org/10.1039/c5cs00564g.
30. Smith R, Wright KL, Ashton L. Raman spectroscopy: an evolving technique for live cell studies. Analyst. 2016;141:3590–600. https://doi.org/10.1039/c6an00152a.
31. Kirkwood TB, Austad SN. Why do we age? Nature. 2000;408:233–8. https://doi.org/10.1038/35041682.
32. Lopez-Otin C, Blasco MA, Partridge L, Serrano M, Kroemer G. The hallmarks of aging. Cell. 2013;153:1194–217. https://doi.org/10.1016/j.cell.2013.05.039.
33. Johnson AA, Stolzing A. The role of lipid metabolism in aging, lifespan regulation, and age-related disease. Aging Cell. 2019;18:e13048. https://doi.org/10.1111/acel.13048.
34. van Meer G, Voelker DR, Feigenson GW. Membrane lipids: where they are and how they behave. Nat Rev Mol Cell Biol. 2008;9:112–24. https://doi.org/10.1038/nrm2330.
35. Bowman AP, et al. Evaluation of lipid coverage and high spatial resolution MALDI-imaging capabilities of oversampling combined with laser post-ionisation. Anal Bioanal Chem. 2020;412:2277–89. https://doi.org/10.1007/s00216-019-02290-3.
36. Murphy RC, Hankin JA, Barkley RM. Imaging of lipid species by MALDI mass spectrometry. J Lipid Res. 2009;50(Suppl):S317-322. https://doi.org/10.1194/jlr.R800051-JLR200.
37. Ugur B, Chen K, Bellen HJ. Drosophila tools and assays for the study of human diseases. Dis Model Mech. 2016;9:235–44. https://doi.org/10.1242/dmm.023762.
38. Chatterjee N, Perrimon N. What fuels the fly: Energy metabolism in Drosophila and its application to the study of obesity and diabetes. Sci Adv. 2012;7. https://doi.org/10.1126/sciadv.abg4336.
39. Chen AJ, et al. Fingerprint stimulated Raman scattering imaging reveals retinoid coupling lipid metabolism and survival. ChemPhysChem. 2018;19:2500–6. https://doi.org/10.1002/cphc.201800545.
40. Hahn O, et al. Dietary restriction protects from age-associated DNA methylation and induces epigenetic reprogramming of lipid metabolism. Genome Biol. 2017;18:56. https://doi.org/10.1186/s13059-017-1187-1.
41. Gao AW, et al. A sensitive mass spectrometry platform identifies metabolic changes of life history traits in C. elegans. Sci Rep. 2017;7:2408. https://doi.org/10.1038/s41598-017-02539-w.
42. Houtkooper RH, et al. The metabolic footprint of aging in mice. Sci Rep. 2011;1:134. https://doi.org/10.1038/srep00134.
43. Hansen M, Flatt T, Aguilaniu H. Reproduction, fat metabolism, and life span: what is the connection? Cell Metab. 2013;17:10–9. https://doi.org/10.1016/j.cmet.2012.12.003.
44. Christian P, Sacco J, Adeli K. Autophagy: emerging roles in lipid homeostasis and metabolic control. Biochim Biophys Acta. 1831;819–824:2013. https://doi.org/10.1016/j.bbalip.2012.12.009.

45. Walther TC, Farese RV Jr. Lipid droplets and cellular lipid metabolism. Annu Rev Biochem. 2012;81:687–714. https://doi.org/10.1146/annurev-biochem-061009-102430.
46. Chung KW. Advances in Understanding of the Role of Lipid Metabolism in Aging. Cells. 2021;10. https://doi.org/10.3390/cells10040880.
47. Li Y, Zhang W, Fung AA, Shi L. DO-SRS imaging of diet regulated metabolic activities in Drosophila during aging processes. Aging Cell. 2022;21:e13586. https://doi.org/10.1111/acel.13586.
48. Templeman NM, Murphy CT. Regulation of reproduction and longevity by nutrient-sensing pathways. J Cell Biol. 2018;217:93–106. https://doi.org/10.1083/jcb.201707168.
49. Piper MD, Partridge L, Raubenheimer D, Simpson SJ. Dietary restriction and aging: a unifying perspective. Cell Metab. 2011;14:154–60. https://doi.org/10.1016/j.cmet.2011.06.013.
50. Simpson SJ, et al. Dietary protein, aging and nutritional geometry. Ageing Res Rev. 2017;39:78–86. https://doi.org/10.1016/j.arr.2017.03.001.
51. Toyoshima Y, et al. Dietary protein deprivation upregulates insulin signaling and inhibits gluconeogenesis in rat liver. J Mol Endocrinol. 2010;45:329–40. https://doi.org/10.1677/JME-10-0102.
52. El Khoury D, Anderson GH. Recent advances in dietary proteins and lipid metabolism. Curr Opin Lipidol. 2013;24:207–13. https://doi.org/10.1097/MOL.0b013e3283613bb7.
53. Rietman A, Schwarz J, Tome D, Kok FJ, Mensink M. High dietary protein intake, reducing or eliciting insulin resistance? Eur J Clin Nutr. 2014;68:973–9. https://doi.org/10.1038/ejcn.2014.123.
54. Nassel DR, Liu Y, Luo J. Insulin/IGF signaling and its regulation in Drosophila. Gen Comp Endocrinol. 2015;221:255–66. https://doi.org/10.1016/j.ygcen.2014.11.021.
55. Bettedi L, Yan A, Schuster E, Alic N, Foukas LC. Increased mitochondrial and lipid metabolism is a conserved effect of Insulin/PI3K pathway downregulation in adipose tissue. Sci Rep. 2020;10:3418. https://doi.org/10.1038/s41598-020-60210-3.
56. Li Y, et al. Direct imaging of lipid metabolic changes in drosophila ovary during aging using DO-SRS microscopy. Front Aging. 2021;2:819903. https://doi.org/10.3389/fragi.2021.819903.
57. Li Y, et al. Bioorthogonal Stimulated Raman Scattering Imaging Uncovers Lipid Metabolic Dynamics in Drosophila Brain During Aging. GEN Biotechnol. 2023;2:247–61. https://doi.org/10.1089/genbio.2023.0017.
58. Li Y, et al. Microglial lipid droplet accumulation in tauopathy brain is regulated by neuronal AMPK. Cell Metab. 2024;36:1351-1370 e1358. https://doi.org/10.1016/j.cmet.2024.03.014.
59. Hinnant TD, Merkle JA, Ables ET. Coordinating proliferation, polarity, and cell fate in the drosophila female germline. Front Cell Dev Biol. 2020;8:19. https://doi.org/10.3389/fcell.2020.00019.
60. Na J, Kim GJ. Recent trends in stem cell therapy for premature ovarian insufficiency and its therapeutic potential: a review. J Ovarian Res. 2020;13:74. https://doi.org/10.1186/s13048-020-00671-2.
61. Katajisto P, et al. Stem cells. Asymmetric apportioning of aged mitochondria between daughter cells is required for stemness. Science. 2015;348:340–3. https://doi.org/10.1126/science.1260384.
62. Tiwari SK, Mandal S. mitochondrial control of stem cell state and fate: lessons from Drosophila. Front Cell Dev Biol. 2021;9:606639. https://doi.org/10.3389/fcell.2021.606639.
63. Duncan FE, Gerton JL. Mammalian oogenesis and female reproductive aging. Aging (Albany NY). 2018;10:162–3. https://doi.org/10.18632/aging.101381.
64. Zhang M, et al. Mitofusin 1 is required for female fertility and to maintain ovarian follicular reserve. Cell Death Dis. 2019;10:560. https://doi.org/10.1038/s41419-019-1799-3.
65. Baddela VS, Sharma A, Vanselow J. Non-esterified fatty acids in the ovary: friends or foes? Reprod Biol Endocrinol. 2020;18:60. https://doi.org/10.1186/s12958-020-00617-9.
66. Choe C, Lademann J, Darvin ME. A depth-dependent profile of the lipid conformation and lateral packing order of the stratum corneum in vivo measured using Raman microscopy. Analyst. 2016;141:1981–7. https://doi.org/10.1039/c5an02373d.
67. Matthews Q, Jirasek A, Lum J, Duan X, Brolo AG. Variability in Raman spectra of single human tumor cells cultured in vitro: correlation with cell cycle and culture confluency. Appl Spectrosc. 2010;64:871–87. https://doi.org/10.1366/000370210792080966.
68. Uematsu M, Shimizu T. Raman microscopy-based quantification of the physical properties of intracellular lipids. Commun Biol. 2021;4:1176. https://doi.org/10.1038/s42003-021-02679-w.
69. Bruce KD, Zsombok A, Eckel RH. Lipid processing in the brain: a key regulator of systemic metabolism. Front Endocrinol (Lausanne). 2017;8:60. https://doi.org/10.3389/fendo.2017.00060.
70. Denis I, Potier B, Heberden C, Vancassel S. Omega-3 polyunsaturated fatty acids and brain aging. Curr Opin Clin Nutr Metab Care. 2015;18:139–46. https://doi.org/10.1097/MCO.0000000000000141.
71. Cutuli D. Functional and structural benefits induced by omega-3 polyunsaturated fatty acids during aging. Curr Neuropharmacol. 2017;15:534–42. https://doi.org/10.2174/1570159X14666160614091311.
72. Janssen CI, Kiliaan AJ. Long-chain polyunsaturated fatty acids (LCPUFA) from genesis to senescence: the influence of LCPUFA on neural development, aging, and neurodegeneration. Prog Lipid Res. 2014;53:1–17. https://doi.org/10.1016/j.plipres.2013.10.002.
73. Tindale LC, Leach S, Spinelli JJ, Brooks-Wilson AR. Lipid and Alzheimer's disease genes associated with healthy aging and longevity in healthy oldest-old. Oncotarget. 2017;8:20612–21. https://doi.org/10.18632/oncotarget.15296.
74. Bailey AP, et al. antioxidant role for lipid droplets in a stem cell Niche of Drosophila. Cell. 2015;163:340–53. https://doi.org/10.1016/j.cell.2015.09.020.
75. Marschallinger J, et al. Lipid-droplet-accumulating microglia represent a dysfunctional and proinflammatory state in the aging brain. Nat Neurosci. 2020;23:194–208. https://doi.org/10.1038/s41593-019-0566-1.
76. Liu L, MacKenzie KR, Putluri N, Maletic-Savatic M, Bellen HJ. The glia-neuron lactate shuttle and elevated ros promote lipid synthesis in neurons and lipid droplet accumulation in Glia via APOE/D. Cell Metab. 2017;26:719-7377 e16. https://doi.org/10.1016/j.cmet.2017.08.024.
77. Olzmann JA, Carvalho P. Dynamics and functions of lipid droplets. Nat Rev Mol Cell Biol. 2019;20:137–55. https://doi.org/10.1038/s41580-018-0085-z.
78. Samuel AZ, et al. Molecular profiling of lipid droplets inside HuH7 cells with Raman micro-spectroscopy. Commun Biol. 2020;3:372. https://doi.org/10.1038/s42003-020-1100-4.
79. Musselman LP, Kuhnlein RP. Drosophila as a model to study obesity and metabolic disease. J Exp Biol. 2018;221. https://doi.org/10.1242/jeb.163881.
80. Musselman LP, et al. A high-sugar diet produces obesity and insulin resistance in wild-type Drosophila. Dis Model Mech. 2011;4:842–9. https://doi.org/10.1242/dmm.007948.

81. Pasco MY, Leopold P. High sugar-induced insulin resistance in Drosophila relies on the lipocalin Neural Lazarillo. PLoS One. 2012;7:e36583. https://doi.org/10.1371/journal.pone.0036583.
82. Woodling NS, Rajasingam A, Minkley LJ, Rizzo A, Partridge L. Independent glial subtypes delay development and extend healthy lifespan upon reduced insulin-PI3K signalling. BMC Biol. 2020;18:124. https://doi.org/10.1186/s12915-020-00854-9.
83. Zadoorian A, Du X, Yang H. Lipid droplet biogenesis and functions in health and disease. Nat Rev Endocrinol. 2023;19:443–59. https://doi.org/10.1038/s41574-023-00845-0.
84. Zhang W, et al. Lipid droplets, the central hub integrating cell metabolism and the immune system. Front Physiol. 2021;12:746749. https://doi.org/10.3389/fphys.2021.746749.
85. Farmer BC, Walsh AE, Kluemper JC, Johnson LA. Lipid droplets in neurodegenerative disorders. Front Neurosci. 2020;14:742. https://doi.org/10.3389/fnins.2020.00742.
86. Litvinchuk A, et al. Amelioration of Tau and ApoE4-linked glial lipid accumulation and neurodegeneration with an LXR agonist. Neuron. 2024;112:2079. https://doi.org/10.1016/j.neuron.2024.05.021.
87. Farmer BC, Kluemper J, Johnson LA. Apolipoprotein E4 alters astrocyte fatty acid metabolism and lipid droplet formation. Cells. 2019;8. https://doi.org/10.3390/cells8020182.
88. Claes C, et al. Plaque-associated human microglia accumulate lipid droplets in a chimeric model of Alzheimer's disease. Mol Neurodegener. 2021;16:50. https://doi.org/10.1186/s13024-021-00473-0.
89. Victor MB, et al. Lipid accumulation induced by APOE4 impairs microglial surveillance of neuronal-network activity. Cell Stem Cell. 2022;29:1197-1212 e1198. https://doi.org/10.1016/j.stem.2022.07.005().
90. Mihaylova MM, Shaw RJ. The AMPK signalling pathway coordinates cell growth, autophagy and metabolism. Nat Cell Biol. 2011;13:1016–23. https://doi.org/10.1038/ncb2329.
91. Garcia D, Shaw RJ. AMPK: mechanisms of cellular energy sensing and restoration of metabolic balance. Mol Cell. 2017;66:789–800. https://doi.org/10.1016/j.molcel.2017.05.032.
92. Steinberg GR, Hardie DG. New insights into activation and function of the AMPK. Nat Rev Mol Cell Biol. 2023;24:255–72. https://doi.org/10.1038/s41580-022-00547-x.
93. Li Z, et al. Multimodal imaging of metabolic activities for distinguishing subtypes of breast cancer. Biomed Opt Express. 2023;14:5764–80. https://doi.org/10.1364/BOE.500252.
94. Fung AA, et al. Imaging sub-cellular methionine and insulin interplay in triple negative breast cancer lipid droplet metabolism. Front Oncol. 2022;12:858017. https://doi.org/10.3389/fonc.2022.858017.
95. Hanahan D. Hallmarks of cancer: new dimensions. Cancer Discov. 2022;12:31–46. https://doi.org/10.1158/2159-8290.CD-21-1059.
96. Bacci M, Lorito N, Smiriglia A, Morandi A. Fat and furious: lipid metabolism in antitumoral therapy response and resistance. Trends Cancer. 2021;7:198–213. https://doi.org/10.1016/j.trecan.2020.10.004.
97. Cheng H, et al. Lipid metabolism and cancer. Life (Basel). 2022;12. https://doi.org/10.3390/life12060784.
98. O'Reilly D, Sendi MA, Kelly CM. Overview of recent advances in metastatic triple negative breast cancer. World J Clin Oncol. 2021;12:164–82. https://doi.org/10.5306/wjco.v12.i3.164.
99. Abramson VG, Lehmann BD, Ballinger TJ, Pietenpol JA. Subtyping of triple-negative breast cancer: implications for therapy. Cancer. 2015;121:8–16. https://doi.org/10.1002/cncr.28914.
100. Contorno S, Darienzo RE, Tannenbaum R. Evaluation of aromatic amino acids as potential biomarkers in breast cancer by Raman spectroscopy analysis. Sci Rep. 2021;11:1698. https://doi.org/10.1038/s41598-021-81296-3.
101. Bagheri P, Hoang K, Fung AA, Hussain S, Shi L. Visualizing cancer cell metabolic dynamics regulated with aromatic amino acids using DO-SRS and 2PEF microscopy. Front Mol Biosci. 2021;8:779702. https://doi.org/10.3389/fmolb.2021.779702.
102. Luo H, et al. Increased lipogenesis is critical for self-renewal and growth of breast cancer stem cells: Impact of omega-3 fatty acids. Stem Cells. 2021;39:1660–70. https://doi.org/10.1002/stem.3452.
103. Burke KA, et al. Second-harmonic generation scattering directionality predicts tumor cell motility in collagen gels. J Biomed Opt. 2015;20:051024. https://doi.org/10.1117/1.JBO.20.5.051024.
104. Cai H, Dong LQ, Liu F. Recent advances in adipose mTOR signaling and function: therapeutic prospects. Trends Pharmacol Sci. 2016;37:303–17. https://doi.org/10.1016/j.tips.2015.11.011.
105. Kitada M, Xu J, Ogura Y, Monno I, Koya D. Mechanism of activation of mechanistic target of rapamycin complex 1 by methionine. Front Cell Dev Biol. 2020;8:715. https://doi.org/10.3389/fcell.2020.00715.
106. Gupta C, Tikoo K. High glucose and insulin differentially modulates proliferation in MCF-7 and MDA-MB-231 cells. J Mol Endocrinol. 2013;51:119–29. https://doi.org/10.1530/JME-13-0062.
107. Borrego SL, et al. Metabolic changes associated with methionine stress sensitivity in MDA-MB-468 breast cancer cells. Cancer Metab. 2016;4:9. https://doi.org/10.1186/s40170-016-0148-6.
108. Jeon H, et al. Methionine deprivation suppresses triple-negative breast cancer metastasis in vitro and in vivo. Oncotarget. 2016;7:67223–34. https://doi.org/10.18632/oncotarget.11615.
109. Gong L, Lin S, Huang Z. Super-resolution stimulated Raman scattering microscopy enhanced by quantum light and deconvolution. Opt Lett. 2023;48:6516–9. https://doi.org/10.1364/OL.509616.
110. Shi L, et al. Super-resolution vibrational imaging using expansion stimulated raman scattering microscopy. Adv Sci (Weinh). 20229:e2200315. https://doi.org/10.1002/advs.202200315.
111. Shou J, et al. Super-resolution vibrational imaging based on photoswitchable Raman probe. Sci Adv. 2023;9:eade9118. https://doi.org/10.1126/sciadv.ade9118.
112. Jang H, et al. Super-resolution SRS microscopy with A-PoD. Nat Methods. 2023;20:448–58. https://doi.org/10.1038/s41592-023-01779-1.
113. Wei M, et al. Volumetric chemical imaging by clearing-enhanced stimulated Raman scattering microscopy. Proc Natl Acad Sci U S A. 2019;116:6608–17. https://doi.org/10.1073/pnas.1813044116.
114. Lombardini A, et al. High-resolution multimodal flexible coherent Raman endoscope. Light Sci Appl. 2018;7:10. https://doi.org/10.1038/s41377-018-0003-3.
115. Lochocki B, et al. Multimodal, label-free fluorescence and Raman imaging of amyloid deposits in snap-frozen Alzheimer's disease human brain tissue. Commun Biol. 2021;4:474. https://doi.org/10.1038/s42003-021-01981-x.
116. Vasquez D, et al. Multimodal scanning microscope combining optical coherence tomography, raman spectroscopy and fluorescence lifetime microscopy for mesoscale label-free imaging of tissue. Anal Chem. 2021;93:11479–87. https://doi.org/10.1021/acs.analchem.1c01637.
117. Crisford A, et al. Harnessing Raman spectroscopy and Multimodal Imaging of Cartilage for Osteoarthritis Diagnosis.

medRxiv. 2023:2023.2009.2005.23294936. https://doi.org/10.1101/2023.09.05.23294936.
118. Jurowski K, Noga M, Kobylarz D, Niżnik Ł, Krośniak A. Multimodal imaging using Raman spectroscopy and FTIR in a Single Analytical Instrument with a Microscope (Infrared Raman Microscopy AIRsight, Shimadzu): opportunities and Applications. Int J Mol Sci. 2024;25:6884.

Authors and Affiliations

Lingyan Shi[1] · Jorge Villazon[1]

✉ Lingyan Shi
L2shi@ucsd.edu

[1] Shu Chien-Gene Lay Department of Bioengineering, University of California San Diego, La Jolla, CA 92093, USA